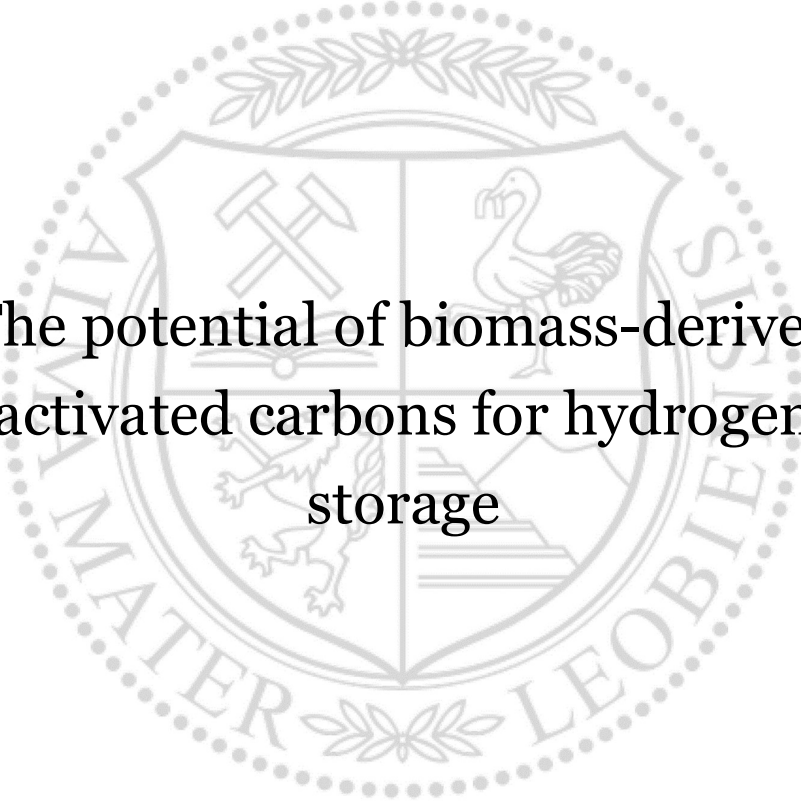




Institute of Physics

Master's Thesis

The background features a large, faint watermark of the Montan Universität Leoben seal. The seal is circular and contains a shield with various symbols: crossed hammers, a stork, a lion, and a building. The text 'MONTAN UNIVERSITÄT LEOBEN' is written around the perimeter of the seal.

The potential of biomass-derived
activated carbons for hydrogen
storage

Sebastian Manfred Stock, BSc.

February 2021



EIDESSTÄTLICHE ERKLÄRUNG

Ich erkläre an Eides statt, dass ich diese Arbeit selbständig verfasst, andere als die angegebenen Quellen und Hilfsmittel nicht benutzt, und mich auch sonst keiner unerlaubten Hilfsmittel bedient habe.

Ich erkläre, dass ich die Richtlinien des Senats der Montanuniversität Leoben zu "Gute wissenschaftliche Praxis" gelesen, verstanden und befolgt habe.

Weiters erkläre ich, dass die elektronische und gedruckte Version der eingereichten wissenschaftlichen Abschlussarbeit formal und inhaltlich identisch sind.

Datum 22.02.2021

Unterschrift Verfasser/in
Sebastian Manfred Stock

Acknowledgements

At first, I want to thank my supervisor Oskar Paris for his advice during the thesis and for giving me the opportunity to pursue my personal scientific interest. It seems that he is multiple persons in one body, as he lets us students to wonder how he can manage all his duties during the day and still has time for detailed scientific discussions. Nevertheless, I am very grateful to be part of his research group and I am very much looking forward to the next three years.

Next, I want to thank my experimental mentor Nikolaos Kostoglou from the Department of Materials Science for teaching me the necessary skills to work in the field of hydrogen storage and for the enlightening late-night calls concerning scientific matters, since those were the only ones I have received in the past year, thanks to COVID-19.

Additionally, I want to thank Stefan Spirk and Julian Selinger from the Institute of Bioproducts and Paper Technology at TU Graz for providing the investigated materials and their support during the thesis. I am also very grateful that I can add something to their research and hope for a continuation of this collaboration. Furthermore, I would like to thank Christian Mitterer from the Department of Materials Science for reviewing my work and for his valuable scientific and writing style input.

I also want to thank my colleagues at the Institute of Physics for their support and for creating a working environment, in which it is a pleasure to go to everyday. Special thanks are directed to Rainer Lechner, who showed me some tricks with the laboratory SAXS device, without which I would probably still sit in the lab. Moreover, I want to thank Gerhard Popovski for his support and for developing the MULIP Carbon CLD software. More or less often, during the preparation of a thesis one has to take some breaks in order to sort the thoughts and it was always a pleasure to spend those breaks with elongated off-topic discussions with Markus Kratzer and Taha Honaramooz. The same accounts for the highly enjoyable talks with Heide Kirchberger und Nadine Aichberger, without which scientific work would probably not be possible at all.

Lastly, I want to thank my family for their support and for guiding me towards the person I am today. And hopefully I can at least give something back to them at some point, knowing that it will never balance what they gave me, the gift of life.

-Mons. Monti non miscetur, at vero homo homini-

To all who accompanied me on the summits in the past year

Abstract

Habits are fundamental parts in every human's life and some of them need to change to make a step forward in slowing down global warming. As oddly as it may sound, the most common habit of enjoying a freshly brewed cup of coffee every morning may contribute to a certain extent to this deceleration. The spent coffee grounds, upon chemical treatment, can be used to store the fuel which can power the cars of the future, namely hydrogen.

Storing hydrogen in activated carbons synthesized from biological waste materials contributes to the solution of the problem in two ways. Firstly, for the transition to a carbon free society the need for electrified vehicles is increasing, which battery-containing cars cannot stem alone. Therefore, hydrogen powered cars, using a fuel cell to generate electricity, are a promising addition to this sector. Those fuel cells need gaseous hydrogen, which can be stored in activated carbons derived from coffee waste. Secondly, the waste can be brought back to new use, thus increasing the sustainability of such a storage system even more.

The structural characteristics of three biomass-derived activated carbons, namely spent coffee grounds, silver skin from coffee beans and fines from paper production, were investigated in this thesis. This was accomplished using Raman spectroscopy, X-ray scattering and gas sorption analysis with different gases. To evaluate the hydrogen storage capacity, low-pressure (0-1 bar) hydrogen adsorption/desorption experiments were conducted at three different temperatures (77, 87 and 97 K). It was found that the pore width, the specific surface area, and the pore volume play an important role in the hydrogen uptake performance. With decreasing mean pore width, the hydrogen uptake at 1 bar and 77 K was found to increase. The sample derived from spent coffee grounds has the highest uptake of 2.81 wt%, followed by the coffee silver skins with 2.77 wt% and 1.47 wt% for the sample synthesized from fines. The first two materials, due to their relatively high uptake at low pressures, have a great potential for an application in hydrogen storage systems operating in cryogenic conditions.

Kurzfassung

Gewohnheiten sind ein grundlegender Bestandteil im Leben eines jeden Menschen und einige von diesen müssen geändert werden, um einen Schritt vorwärts bei der Verlangsamung der globalen Erwärmung zu machen. So seltsam es auch klingen mag, die häufigste Angewohnheit, jeden Morgen eine frisch gebrühte Tasse Kaffee zu genießen, kann in gewissem Maße zu dieser Verlangsamung beitragen. Der verbrauchte Kaffeesatz kann nach chemischer Behandlung zur Speicherung des Treibstoffs der Zukunft verwendet werden, nämlich Wasserstoff.

Die Speicherung von Wasserstoff in aktivierten Kohlenstoffen, die aus biologischen Abfallstoffen synthetisiert werden, trägt in zweierlei Hinsicht zur Lösung des Problems bei. Erstens steigt für den Übergang zu einer kohlenstofffreien Gesellschaft der Bedarf an elektrifizierten Fahrzeugen, den batteriebetriebene Autos allein nicht stemmen können. Daher sind wasserstoffbetriebene Autos, die eine Brennstoffzelle zur Stromerzeugung nutzen, eine vielversprechende Ergänzung in diesem Bereich. Diese Brennstoffzellen benötigen gasförmigen Wasserstoff, der in Aktivkohle gespeichert werden kann. Zum anderen können die Abfälle wieder einer neuen Nutzung zugeführt werden, was die Nachhaltigkeit eines solchen Speichersystems noch weiter erhöht.

In dieser Arbeit wurden die strukturellen Eigenschaften von drei biologisch gewonnenen Aktivkohlen, nämlich verbrauchter Kaffeesatz, Silberhäutchen von Kaffeebohnen und Feinanteile aus der Papierproduktion, untersucht. Dies erfolgte durch den Einsatz von Raman-Spektroskopie, Röntgenstreuung und Gassorptionsanalyse mit verschiedenen Gasen. Um die Wasserstoffspeicherkapazität zu bewerten, wurden Niederdruck-Wasserstoffsorptionsexperimente bei drei verschiedenen Temperaturen (77, 87 und 97 K) durchgeführt. Es wurde festgestellt, dass die Porenweite, die spezifische Oberfläche und das Porenvolumen eine wichtige Rolle für die Wasserstoffaufnahme spielen. Mit abnehmender mittlerer Porenweite stieg die Wasserstoffaufnahme bei 1 bar und 77 K an. Die aus Kaffeesatz gewonnene Probe hat die höchste Aufnahme von 2,81 Gew.-%, gefolgt von der Kaffeesilberhaut mit einer Aufnahme von 2,77 Gew.-% und 1,47 Gew.-% für die aus Feinanteilen synthetisierte Probe. Die ersten beiden Materialien weisen aufgrund

ihrer relativ hohen Wasserstoffaufnahme bei niedrigen Drücken ein großes Potenzial für eine Anwendung in Wasserstoffspeichern auf.

Abbreviations

AC	activated carbon
BET	Brunauer-Emmett-Teller
CLD	chord length distribution
CNT	carbon nanotube
DFT	Density Functional Theory
DOE	Department of Energy
EOS	equation of states
FL	Freundlich-Langmuir
FWHM	full width at half maximum
GCMC	Grand Canonical Monte Carlo
GRF	Gaussian Random Fields
GSA	gas (ad)sorption analysis
IUPAC	International Union of Pure and Applied Chemistry
LJ	Lennard-Jones
MOFs	metal organic frameworks
PSD	pore size distribution
QSDFE	Quenched Solid Density Functional Theory
SAXS	small-angle X-ray scattering

SSA	specific surface area
STP	standard temperature and pressure
TPV	total pore volume
vdW	Van der Waals
WAXS	wide angle X-ray scattering
XRD	X-ray diffraction

Table of content

Acknowledgements	ii
Abstract	v
Kurzfassung.....	vi
Abbreviations	viii
1 Motivation	1
2 Fundamentals	3
2.1 Hydrogen storage.....	3
2.1.1 Hydrogen storage challenge	4
2.1.2 Hydrogen storage technologies.....	5
2.1.3 Hydrogen storage materials	9
2.2 Hydrogen storage in porous materials.....	12
2.2.1 Fundamentals of physisorption.....	14
2.2.2 Structure of nanoporous activated carbons	19
2.2.3 Hydrogen storage in nanoporous activated carbons	22
2.3 Interaction of X-rays with matter	26
2.3.1 Small-angle X-ray scattering on nanoporous carbons.....	27
2.3.2 Wide-angle X-ray scattering on nanoporous carbons	32
3 Experimental methods.....	35
3.1 Carbon materials and synthesis	35
3.2 Materials characterization.....	36
3.2.1 Gas sorption analysis and hydrogen sorption experiments.....	36
3.2.2 Raman spectroscopy	37
3.2.3 X-ray Scattering	38

4	Results and Discussion	40
4.1	Structural parameters obtained by Raman spectroscopy.....	40
4.2	Structural parameters obtained by gas sorption analysis.....	44
4.3	Structural parameters obtained by X-ray scattering	49
4.3.1	Wide angle X-ray scattering.....	49
4.3.2	Small-angle X-ray scattering	52
4.4	Hydrogen storage in biomass-derived activated carbon materials	58
4.4.1	Hydrogen uptake performance at different temperatures.....	58
4.4.2	Isosteric enthalpy of adsorption.....	61
4.5	Hydrogen uptake and structural parameters.....	63
4.5.1	Gas adsorption analysis and hydrogen uptake	63
4.5.2	Characteristic lengths and hydrogen uptake	66
4.6	Conclusions.....	68
5	Summary and outlook.....	69
6	Bibliography	71

1 Motivation

Over the last 60 years, humankind has experienced an increase of about 260 % in the number of its members. At the same time frame, the worldwide CO₂ emission has increased roughly by about 400%, from 9344 Mio. t in 1960 to 36573 Mio. t in the year 2018. Although this increase in emission was accompanied by an increase of wealth in the western world, it is a threat to the fragile balance of earth's climate system (here the fragility refers to the climatic conditions that ensure human survival). The effects of global warming due to emissions of greenhouse gases are already noticeable all around the world and the scientific community has come to common concise about how precarious the situation is. Therefore, in the year 2015, the United Nations agreed to keep the long-term increase of the average temperature on earth below 2 °C and in order to servilely reduce the consequences of global warming, below 1.5 °C [1]. To achieve this goal, the annual greenhouse gas emissions have to be lowered by a tremendous amount in the next centuries [2]. This means, that the energy source to fuel our economies and the increasing wealth around the world needs to become carbon free. Unfortunately, there is no perfect stand-alone substitute for carbon rich fuels and therefore these goals can only be achieved by a combination of many different sources of energy [3]. Wind, water, geo-thermal and solar power are established energy sources and contribute about 18 % of the total energy supply in the European Union as of the year 2018 [4]. Those renewable energy sources heavily rely on the climatic conditions and energy can only be harvested when those conditions are met. This however results in the need of sophisticated storage of this electrical energy. Batteries and supercapacitors can store electric energy directly, but in order to meet the requirements of a CO₂-free society, other options must also be considered. One promising way could be the use of this electric power to separate water into hydrogen and oxygen gas and to use the reverse process to generate electricity when needed. However, the produced hydrogen gas, which is the energy carrier, needs to be somehow stored. Different hydrogen storage techniques are already available and carbon materials could play an important role for automotive applications, as they could be incorporated in pressurized-gas storage systems. These nanoporous carbons can be

produced from different precursors, but to enhance the sustainability of such hydrogen storage systems it would be preferable to synthesize them from organic wastes.

In Austria every citizen consumes on average about 6.65 kg of coffee per year and this adds up to a total of around 60000 t of spent coffee grounds [5]. The coffee waste needs to be chemically treated for use in various technical applications or burnt in order to make use of its high calorific power [6]. The same accounts for the coffee silver skin, which is a by-product of the coffee bean roasting process. The evaluation of the potential of different bio-derived activated carbons for hydrogen storage applications accompanied by the fundamental physics of hydrogen storage and the used experimental methods, are the subject of research in the following thesis.

2 Fundamentals

2.1 Hydrogen storage

The human body consists of roughly $3.7 \cdot 10^{27}$ hydrogen atoms, making it not only the most abundant chemical element in the universe, but also in living organisms. Hydrogen is the simplest and lightest element and occurs most commonly as protium (^1H), which consists of an electron and a proton. Deuterium (^2D or D) and tritium (^3H or T) possess one and two neutrons in the nucleus, respectively. The monoatomic isotopes form covalently bonded diatomic molecules, with the molecular formula H_2 . At standard temperature and pressure (STP) conditions ($0\text{ }^\circ\text{C}$ or 273 K and 100 kPa or 1 bar), hydrogen is a colorless, odorless, tasteless, non-toxic, non-metallic and highly flammable gas [7,8]. H_2 is found in various chemical substances, as in H_2O and covalently bonded organic compounds (natural gas and oil), or as an anion (H^-) or cation (H^+) in ionic compounds and also exhibits a metal-like behavior in intermetallic compounds [9]. It exhibits a very small volumetric density of 0.084 kg/m^3 at STP conditions and additionally a low boiling and melting point of $-252.8\text{ }^\circ\text{C}$ (or 20.3 K) and $-259\text{ }^\circ\text{C}$ (or 14 K) at 1 bar , respectively, as displayed in Fig. 2.1.

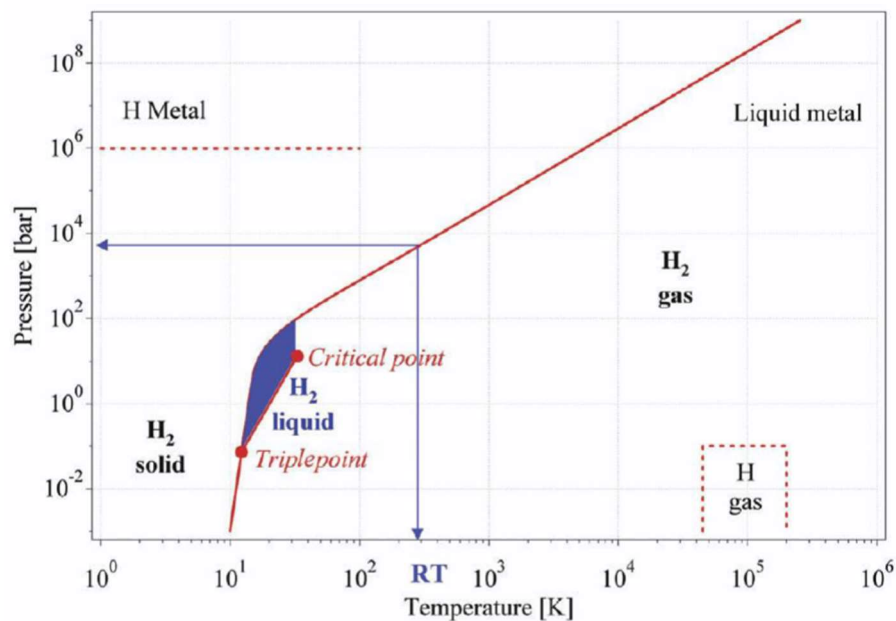


Fig. 2.1: Primitive phase diagram for hydrogen. Adapted from [7,9] and with permission from Springer.

The triple point of hydrogen is found at 13.8 K and 0.07 bar, at which the three states (i.e. gas, liquid and solid) coexist in thermodynamic equilibrium. Hydrogen can be liquid from its triple point up to 32.9 K (critical point) upon increasing pressure to ~ 12.87 bar. At these conditions liquid hydrogen exhibits a density of 70.8 kg/m^3 , which is around 780 times higher than its gas form at ambient conditions. The critical point defines the temperature and pressure above hydrogen can only exist as a gas. Strong repulsive interactions of H_2 molecules are responsible for the low critical point [9]. The underlying challenge of hydrogen storage is the reduction of the enormous volume of hydrogen at ambient conditions (i.e. 1 kg of H_2 takes at STP a volume of $\sim 11 \text{ m}^3$). This can either be achieved by applying work to compress the gas or cooling it below the critical point or by reducing the strong repulsive forces of the molecules by interaction with other materials. Additionally, the storage efficiency, reversibility and price compared to fossil fuels are still an obstacle to the widespread use of hydrogen as a fuel.

2.1.1 Hydrogen storage challenge

The transition from fossil fuels to renewable energy sources can only be accomplished by the development of new energy storage materials and efficient technologies. Especially the automotive industry is relying on new onboard storage systems, as the current battery systems are harmful to the environment during production and after the lifecycle [10,11]. The use of fuel cells to power cars is gaining more attention by the industry, which in return requires sophisticated hydrogen storage technologies to fulfill the demands regarding safety and achievable range [12]. The US Department of Energy (DOE) defined criteria for onboard hydrogen storage systems. The target in gravimetric system storage capacity is 4.5 wt% (1.5 kWh/kg) for the year 2020 and is set to 5.5 wt% (1.8 kWh/kg) by 2025 [8]. The systems should operate at a minimum delivery pressure of 5 bar and a maximum of 12 bar with the delivery temperature ranging between $-40 \text{ }^\circ\text{C}$ and $85 \text{ }^\circ\text{C}$. The systems filling time should range from 3 to 5 min and withstand at least 1500 filling cycles (from 25 % to full). The minimum system volumetric capacity target is set to 30

g (H₂)/L (1 kWh/L) and to 40 g (H₂)/L (1.3 kWh/L), for the year 2020 and 2025, respectively. Although a variety of different storage systems and materials are available, the proposed target values cannot be satisfied by any current material known [13,14]. Besides the targets for the upcoming years, the DOE also defined “ultimate” targets for hydrogen storage systems, as 0.065 kg (H₂)/kg (system) or 6.5 wt% and 0.005 kg (H₂)/L (system) for gravimetric and volumetric system capacity, respectively. The stated targets refer to complete systems including tank, regulators, piping, valves, insulations, material, cooling system and other components [8]. Additionally, all the capacity targets are based on hydrogen’s lower heating value (LHV) of 33.3 kWh/kg (or 120 MJ/kg). The available storage techniques, different storage materials and potential materials to fulfill the requirements are outlined in the following sections.

2.1.2 Hydrogen storage technologies

The available hydrogen storage technologies may be classified based on their reversibility, operating conditions and storage mechanism. The switching ability between hydrogenation and dehydrogenation of a system leads to a differentiation in reversible or non-reversible storage systems [7]. The required operation temperature (cryogenic, ambient or elevated) and pressure (atmospheric or higher) can be used to distinguish between storage systems. The mechanism of storing and releasing hydrogen gas can be discriminated in physical hydrogen storage via liquefaction, compression or cryo-compression and materials-based storage, which further splits into hydrogen storage via absorption/chemical storage and physisorption, as shown in Fig. 2.2 [7,12,15].

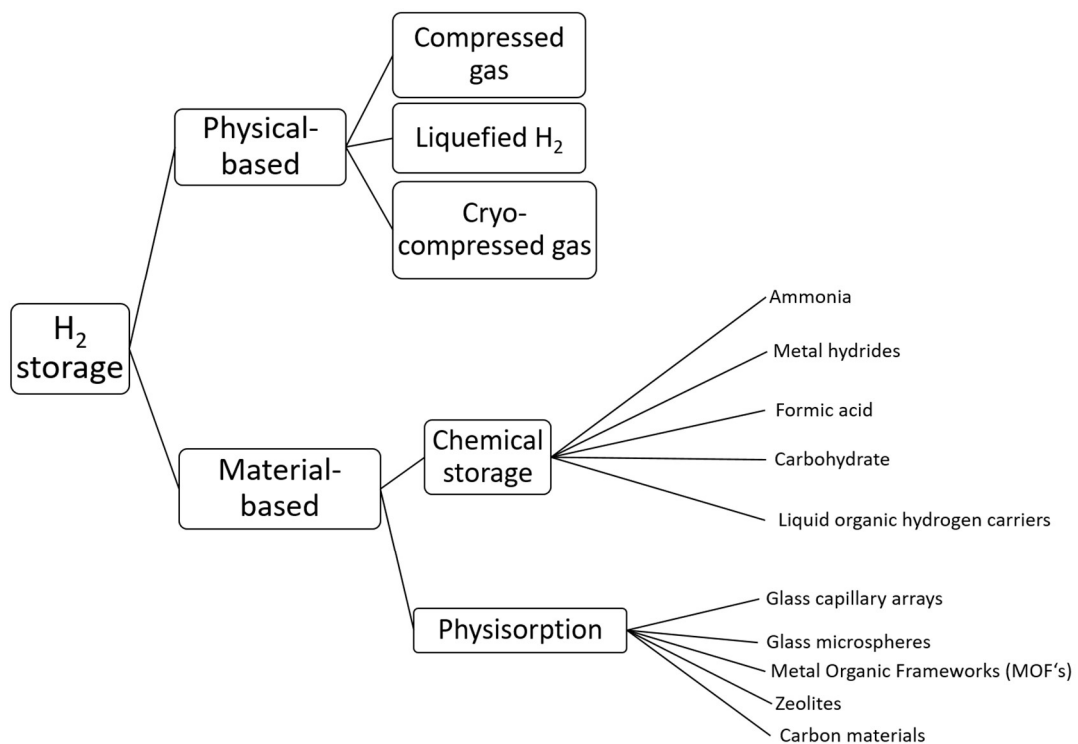


Fig. 2.2: Hydrogen storage methods. Adapted from Ref. [12]. Not all shown H_2 storage possibilities are discussed in the thesis.

The first main group of physical storage methods is discussed in the following, whereas section 2.1.3 is dedicated to material-based hydrogen storage.

Compressed H_2 storage:

The physical storage in the form of pressurized gas is favorable for room temperature storage. However, the gas has to be pressurized up to 700 bar (70 MPa) to achieve useful storage capacities. Thus, strong vessel materials are needed to withstand these high pressures and ensure safety when used in portable systems. The gravimetric system capacity of pressure tanks is limited by the weight of the vessels. As the pressure increases, the thickness of the tank walls increases and therefore the mass. Different types of pressure vessels are readily available to store hydrogen gas. Full metallic vessels can withstand high pressures and are the least expensive, but also the heaviest type, which

limits the wall thickness and thus the tolerable pressures (50 bar) to achieve a low system weight. In comparison, polymer based composites can reduce the system weight and withstand higher pressures up to 100 MPa. They commonly consist of high density polyethylene (HDPE) liners and carbon-reinforced composites to carry the structural load [12]. The gravimetric energy density of hydrogen at 700 bar, based on the LHV (~120 MJ/kg), is around 6 MJ/kg (system), which is 7 times lower compared to conventional gasoline [8,15]. Another issue is the space occupied by such vessels of around 40 L/kg H₂, which limits the amount of usable fuel for electromotive applications [13].

Liquefied hydrogen (LH₂):

In order to liquefy hydrogen under atmospheric pressure, the gas needs to be cooled below the boiling point of 20.3 K, which requires between 30-35 % of the hydrogen's energy content [16]. This is approximately three times the energy needed to compress the gas to 700 bar. Although the volumetric energy density of liquefied hydrogen (8 MJ/L) is higher than compressed gas (~3MJ/L), there are many issues regarding portable applications. Firstly, to maintain the liquid state it must be kept in a multilayered highly isolated vessel. Secondly, LH₂ evaporates very quickly during refueling and it pressurizes easily. Therefore, a tank system has to be vented regularly in case of non-use, in order to prevent boil-off losses [16]. Losses smaller than 0.5% per day can be expected, depending on the size and shape of the tank [13]. Thirdly, the volumetric energy density is considerably smaller compared to conventional gasoline of around 32 MJ/L [16].

Cryo-compressed hydrogen:

Another way to store hydrogen gas is realized by a combination of compression under cryogenic conditions. Such hybrid tanks may contain pressurized LH₂, cooled-compressed gas or a two-phase system of liquid-vapor hydrogen [16]. In case of compressed liquid hydrogen, the density of LH₂ at 21 K increases from 70 g/L at 1 bar to 87 g/L at 240 bar. This could yield a gravimetric system capacity of 6.5 wt% or equivalent volumetric energy density of 5.7 MJ/L (system), which would meet the ultimate target values for

gravimetric system capacity [8,16]. Cooling compressed hydrogen gas can significantly lower the pressures needed to store hydrogen gas, i.e. the pressure can be reduced by 80 % if the system is cooled to 77 K (boiling point of nitrogen) compared to room temperature [16]. The incorporation of adsorbents (activated carbons) further decreases the storage pressures and increases the gravimetric system storage capacity. A theoretical work showed that an activated carbon has to exceed 10.7 wt% (theoretical BET area of 6824 m²/g) in gravimetric material capacity in order to achieve a gravimetric system capacity of 4.5 wt% at 100 bar and 100K. Increasing the heat conductivity of the activated carbon could reduce the needed gravimetric capacity of the activated carbons to 9.8 wt% (BET area: 6222 m²/g) [17]. A schematic representation of a tank system with incorporated activated carbons and an integrated cooling system is shown in Fig. 2.3.

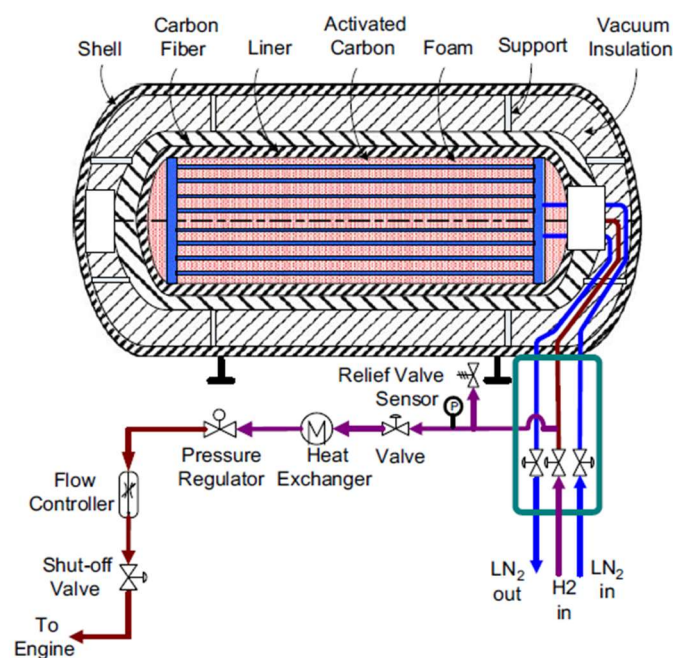


Fig. 2.3: Schematic representation of an on-board cryo-adsorption system. The model tank consists of an aluminum shell, multi-layer vacuum super insulation, carbon-fiber in resin, an aluminum liner and activated carbon mixed with aluminum foam to ensure sufficient heat removal and supply during hydrogenation and dehydrogenation, respectively [17]. Reproduced with permission from Elsevier.

However, such cryo-adsorption system cannot exceed the gravimetric system capacity of a cyro-compressed H_2 gas at the same conditions [17]. Therefore, materials with high surface areas and high H_2 binding energies are needed, which are the subject of the following section.

2.1.3 Hydrogen storage materials

The second main group of hydrogen storage systems is based on materials, so called solid-state hydrogen storage, as shown in Fig. 2.2 [18,19]. Great scientific efforts have been made to study the storage and release of hydrogen in various materials [9,13,14,20]. The solid-state hydrogen storage can be divided into chemical interactions of hydrogen with the host materials and into physisorption of hydrogen in porous materials. Fig. 2.4 gives an overview of different storage materials and their observed gravimetric uptake, as well as the corresponding temperature of hydrogen release and sorption, respectively. As evaluated in the previous section, a potential storage material must exceed the DOE target values in gravimetric uptake in order to surpass these targets when integrated in a storage system [21].

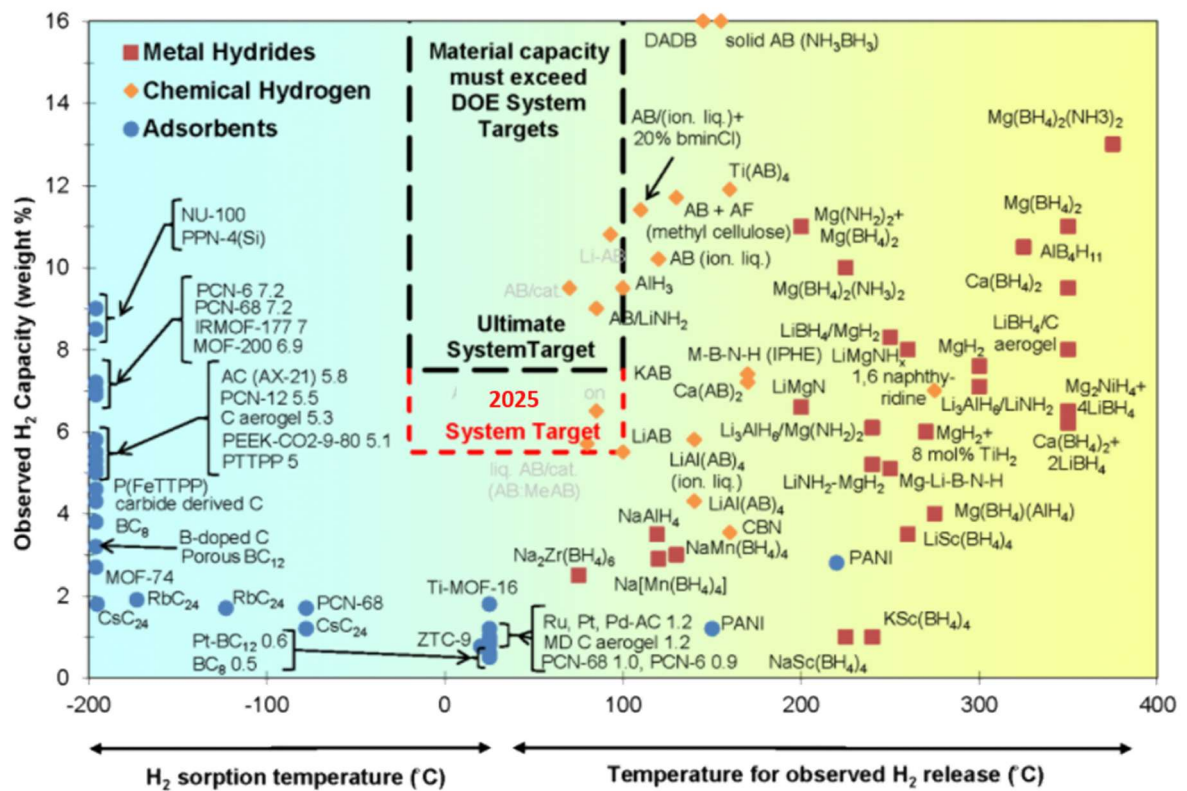


Fig. 2.4: Overview of materials-based hydrogen storage. The graph includes the observed H₂ capacity in wt%, the corresponding sorption temperature and the H₂ release temperature for adsorbents and chemical hydrogen storage materials, respectively [21]. The graph has been adapted to show the target value for the year 2025.

In the following pages, selected chemical hydrogen storage materials and two main material groups for storage via physisorption are briefly discussed. The focus of this work lies on the hydrogen storage capacity of nanoporous carbons, which are discussed in section 2.2.3.

Chemical storage materials:

Hydrogen can be stored chemically in different ways, all of them include hydrogen being bonded chemically to other substances. The variety of chemical compounds is very broad (see Fig. 2.4) and therefore only a few examples are picked out. Nitrogen-containing hydrides exhibit high hydrogen contents. Ammonia or NH₃ has a hydrogen content of

17.7 wt% [16]. The already existing infrastructure is an advantage for this substance, but catalysts (mostly ruthenium) and high temperatures are necessary to release the hydrogen (reaction (2.1)). The reaction of ammonia and lithium hydride could yield 8.1 wt% hydrogen at ambient conditions, which makes it a suitable candidate for use in fuel cell powered cars. The reaction (2.2) is also reversible at high temperatures and pressures.



Another interesting substance is ammonia borane (NH_3BH_3) due to a hydrogen content of 19.6 wt%. Unfortunately, the hydrogen is only released at high temperatures (~ 473 K) and its decomposition results in hazardous substances. A potential solution to this issue is the reaction with metals, water or alcohol at lower temperatures, but yields a lower amount of hydrogen gas [16].

Chemical hydrogen absorption:

Metals can incorporate atomic hydrogen in their crystal structure by absorption and diffusion of dissociated H_2 molecules into the bulk material, usually accompanied by the release of heat. This reaction occurs usually between 3 and 30 bar and at moderate temperatures [9,15]. Metal hydrides can be generally divided into two groups. Binary hydrides contain one metal and hydrogen with a chemical formula MH_x (M=metal, e.g. Mg) and intermetallic hydrides, which contain two or more metals with the chemical formula $A_mB_nH_x$, whereas A (e.g. Ca, Ti, Y, Zr, etc.) and B (e.g. Cr, Mn, Fe, Co, Ni) representing strong and weak hydride elements, respectively [9,15]. Depending on the metals in the compound, they can store between 1.4 and 7.6 wt% of hydrogen and operate between room temperature and 600 K [15]. The major problem for the efficient use of metal hydrides in storage applications is, on the one hand, the low hydrogen content in intermetallic compounds and the high temperatures needed to release hydrogen, accompanied with slow kinetics of lightweight metal hydrides on the other hand [13,16].

Nanoconfinement of hydrides in various porous scaffolds (e.g. carbon nanotubes, activated carbons, zeolites and metal-organic frameworks) could enhance the kinetics by enlarging the reactive surface [22]. Zeolites are naturally occurring inorganic matter, which are built from TO_4 (T is commonly Si or Al) tetrahedra that share oxygen atoms with four TO_4 in their neighborhood [23]. Strictly speaking, zeolites store hydrogen in their well-defined porous structure via physisorption, but a detailed description would expand beyond the scope of this work. Similarly, metal-organic frameworks (MOFs) should be mentioned shortly. They are coordination networks of metal complexes with multi-functional organic ligands, which link the structure [13,23]. MOFs show complex structures and can exhibit up to 7.1 wt% H_2 uptake at 77 K and 40 bar [23]. The structure and the mechanisms to store hydrogen in porous carbon materials will be subject in the following pages.

2.2 Hydrogen storage in porous materials

Before exploring a detailed description of hydrogen storage in nanoporous carbons, some relevant terms and concepts to classify pores have to be highlighted. The term nanopore accounts in general for pores with a diameter or distance between pore walls (or just pore width) lower than 100 nm, according to the International Union of Pure and Applied Chemistry (IUPAC). Nanopores can be further classified into macropores (> 50 nm), mesopores (2 – 50 nm) and micropores (< 2 nm) [24]. A subdivision of micropores into narrow micropores (e.g. ultra-micropores) with a width < 0.7 nm and wider micropores (e.g. super-micropores) is also useful for further discussion. Pores can occur in different geometries and shapes, as shown in Fig. 2.5. Most commonly, the term “pore size” refers to the diameter of cylindrical pores or the width of slit-like pores.

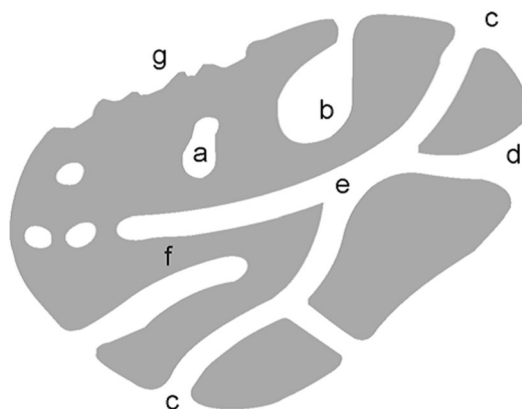


Fig. 2.5: Schematic representation of different pore geometries of a porous solid. (a) closed pore, (b) ink-bottle shape, (c) open cylindrical, (d) funnel-shaped, (e) connection point of different pores to the external surface, (f) closed end cylindrical and (g) external rough surface. Reproduced from Ref. [25]

According to IUPAC, adsorption is defined as the enrichment of molecules, atoms or ions near an interface [24]. The adsorbed substance is known as the adsorbate, whereas the adsorptive is the same substance in fluid phase. The space occupied by the adsorbate is referred to as adsorption space. In general, one can distinguish between physical and chemical adsorption, known as physisorption and chemisorption, respectively. The latter is not the subject of the present work and therefore it only should be mentioned that chemisorption involves the formation of chemical bonds. Physisorption occurs whenever an adsorbable gas (adsorptive) is brought into contact with a solid surface (adsorbent). The term adsorption (isotherm) denotes the increase of adsorbed molecules, whereas desorption (isotherm) denotes the reverse process. The experimentally evaluated adsorbed amount of a substance is defined as the surface excess amount n_{excess} . The excess amount is related to the amount of gas present at the same conditions (n_{total}) in the absence of adsorption via:

$$n_{excess} = n_{total} - \rho_g \cdot V_a, \quad (2.3)$$

where ρ_g is the constant bulk density and V_a is the volume of the adsorbed phase, which cannot be experimentally determined [26,27]. However, at sufficiently low pressures (~ 1 bar) and temperatures (\sim boiling point of adsorptive), n_{excess} corresponds to n_{total} [24,26]. At constant temperature, the relation between the excess amount and the equilibrium pressure of the gas is known as the adsorption isotherm. It is usually presented as the excess amount versus the relative pressure P/P_0 (i.e. P_0 is the saturation vapor pressure) for temperatures below the critical point. If measurements are conducted above the critical point (as in the case of hydrogen gas adsorption measurements) one must use the equilibrium pressure, as no condensation occurs.

2.2.1 Fundamentals of physisorption

Interactions of gas molecules with a solid surface, or with each other, depend on the type of molecules and atoms. The physical adsorption of H_2 on a solid surface is governed by weak van der Waals forces, which include attractive London dispersion forces and short-range repulsive forces. The former arises from rapidly oscillating dipoles, due to fluctuations of the electron cloud within an atom, and in phase coupling of dipoles of neighboring atoms or molecules, which results in a net attractive potential [26]. This description of interaction also leads to the understanding of liquefaction and solidification of a substance. The latter can be identified as the so called Born-repulsion, which limits the distance between two atoms, as it is forbidden for two particles to occupy the same quantum state. Such interaction potentials ϕ of atoms separated by a distance r_{ij} are often modeled by the following general expression:

$$\phi(r_{ij}) = 4 \cdot \epsilon_{ij} \cdot \left[\left(\frac{\sigma_{ij}}{r_{ij}} \right)^m - \left(\frac{\sigma_{ij}}{r_{ij}} \right)^n \right], \quad (2.4)$$

where ϵ_{ij} and σ_{ij} are potential parameters. The negative sign accounts for attractive forces and the positive sign for short-range repulsive forces. The exponents m and n may vary for interactions of different atoms or molecules and are the key parameters to adjust

in order to find physical meaningful interaction potential of real structures [28]. The most prominent interaction potential is the so called Lennard-Jones (LJ) potential, derived from the van der Waals equation of state (EOS) [29]. The resulting potential energy as a function of the distance exhibits a minimum at a certain distance from the surface, which for H_2 is around the radius of the molecule [9]. For hydrogen physisorption this energy is in the range of 1-10 kJ/mol (or 0.01 to 0.1 eV/molecule) and depends on the kind of host material. These interactions lead to basically four different stages of physisorption in porous materials, as illustrated in Fig. 2.6.

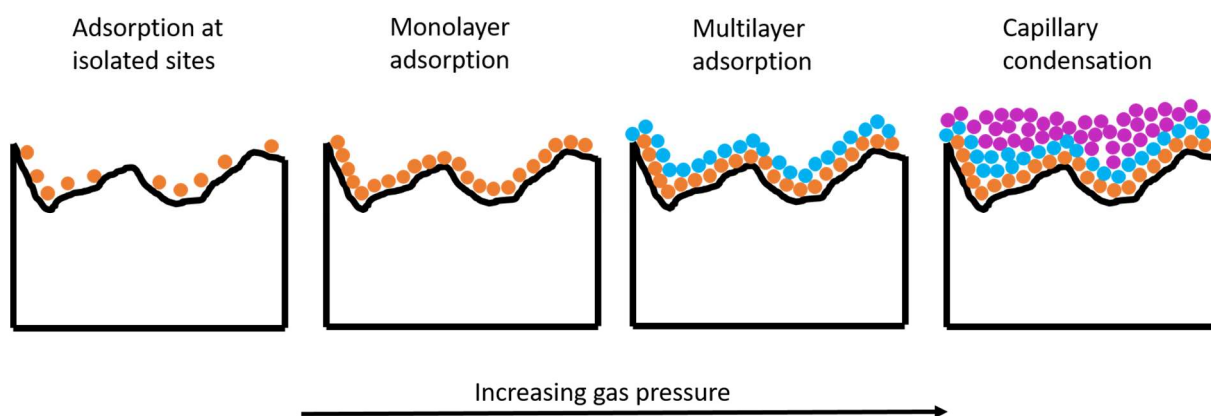


Fig. 2.6. Stages of physisorption by increasing pressure below the critical point. Orange dots represent the molecules, which form the monolayer, blue dots the second layer and purple dots the condensed phase. Adapted from Ref. [7] (own work).

At very low pressures ($\sim 10^{-6}$ mbar typical for a gas sorption experiment), the micropores (pore widths < 2 nm) of the material are getting filled with gas molecules, which is known as micropore filling. This process differs from the one in wider pores as shown in Fig. 2.6, and is governed by spontaneous filling of the available pore space. For wider pores and increasing pressure, the molecules are able to form a dense single layer on the internal surface of meso- and macropores, as well on the external surface (monolayer adsorption). If the temperature is below the critical point of the gas, interactions between the molecules are gaining importance, which eventually leads to the formation of multiple

layers of adsorbate along the surface, commonly referred to as multilayer adsorption. Furthermore, the molecules adsorbed in the mesopores can also condense into a liquid-like phase, which is called capillary condensation. In mesopores the gas-liquid phase transition takes place below the bulk liquid condensation pressure, i.e. at $P/P_0 < 1$. These mechanisms and corresponding pore structures are also reflected in isotherms, of which the IUPAC recommendations identify six characteristic types, as shown in Fig. 2.7 [24].

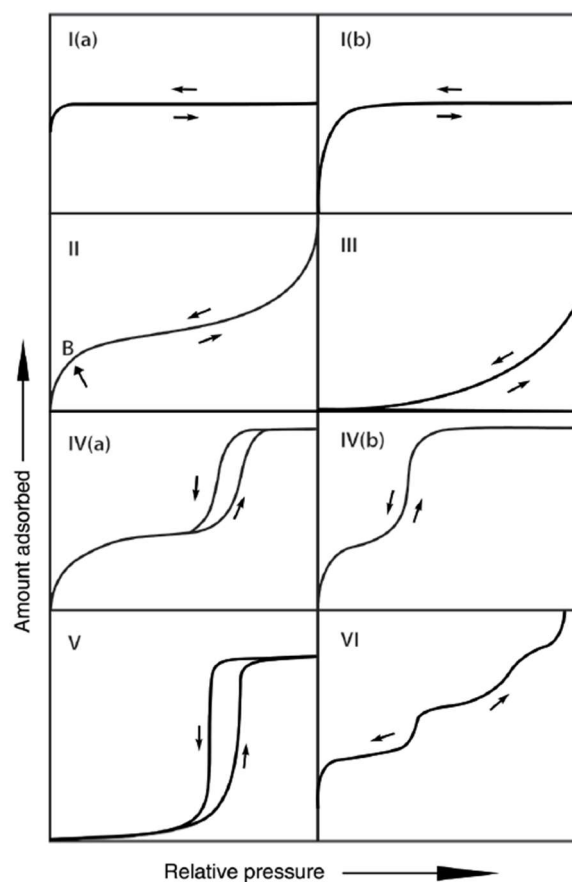


Fig. 2.7: Classification of physisorption isotherms I – VI according to IUPAC. Reprinted from Ref. [24]

Reversible Type I isotherms are observed in purely microporous materials, which have a relatively small external surface area (e.g. activated carbons). The adsorbed amount approaches a finite value at low P/P_0 , which is attributed to the accessible micropore volume rather than the internal surface area. The step uptake at very low relative

pressures is related to strong adsorbent-adsorptive (e.g. solid-gas) interactions in narrow micropores (micropore filling). For nitrogen and argon adsorption at 77 K and 87 K, respectively, such type I(a) isotherm is observed in microporous materials with pore widths mainly < 1 nm [24]. Type I(b) isotherms are given by materials with pore widths < 2.5 nm. For hydrogen adsorption only type I isotherms occur, when measured above the critical point (32.9 K), which is the case in the present work. Type IV(a) isotherms are also of interest, due to a difference in adsorption and desorption, which is called hysteresis loop. As discussed earlier, increasing interactions between molecules can lead to pore condensation, which together with nucleation of the liquid phase during adsorption, results in a hysteresis. Generally, such a type of isotherm is observed in mesoporous materials and is determined also by adsorbent-adsorptive interactions. A further analysis of the different isotherm types is omitted at this point as they have not been observed in the present work. But one could find a detailed description in references [24] and [26]. From the experimentally obtained isotherms many properties of the pore structure of the material can be calculated. A widely used method to extract the specific surface area (SSA) originates from the work of Brunnauer, Emmet and Teller and is abbreviated as BET-method [26]. It relies on a few assumptions of the adsorption process: 1) adsorption takes place on a homogenous surface, 2) the heat of adsorption accounts for the first layer and the heat of condensation for the rest of the layers, 3) interaction between those layer molecules are neglected, 4) the upper most layer is in equilibrium with the gas phase and 5) the number of layers becomes infinite in saturation pressure [7]. The linear form of the BET equation is given by:

$$\frac{1}{W \cdot \left[\left(\frac{P_0}{P} \right) - 1 \right]} = \frac{1}{W_m \cdot C} + \frac{(C - 1)}{W_m \cdot C} \cdot \left(\frac{P}{P_0} \right) \quad (2.5)$$

Here, W is the weight of the adsorbed gas at a relative pressure P/P_0 , W_m is the weight of the adsorbate forming the monolayer coverage and C is a constant which accounts for adsorbent-adsorbate interactions in the first adsorbed layer. By plotting the term on the

left side of the equation (2.5) versus the relative pressure in a range of $0.05 < P/P_0 < 0.35$ for meso- and macroporous materials and $P/P_0 < 0.01$ for microporous materials [7]. Through linear fitting of at least three points, one can obtain the slope (s) and the intersect (i), which relate to W_m . With this value it is possible to calculate the BET area (S_{BET}), as shown in equation (2.6):

$$S_{BET} = \frac{N \cdot A_{CS}}{M \cdot W} \cdot \frac{1}{s + i} = \frac{N \cdot A_{CS} \cdot W_m}{M \cdot W} \quad (2.6)$$

Here, N is the Avogadro number, A_{CS} is the cross-sectional area of the adsorbate molecule and M is the molecular weight. Another approach to determine the SSA is via the generalized adsorption isotherm (GAI) using Quenched Solid Density Functional Theory (QSDFT) (or any other molecular simulation method) for slit-pore geometries. In this model, the adsorption isotherm is fitted with the assumption that the investigated material consists of different pores with varying size and is therefore a sum of these. The GAI can be expressed as:

$$N\left(\frac{P}{P_0}\right) = \int_{W_{min}}^{W_{max}} N\left(\frac{P}{P_0}, W\right) f(W) dW, \quad (2.7)$$

where $N\left(\frac{P}{P_0}\right)$ represents the measured adsorption data, W is the pore width and $f(W)$ is the pore size distribution (PSD) function. With this method it is possible to obtain the PSD and the total pore volume (TPV). Before continuing the discussion on hydrogen storage in nanoporous carbons, a closer look on their structural features is given in the following pages.

2.2.2 Structure of nanoporous activated carbons

Carbon is found in various allotropes and at least since the discovery of the steam engine was the driving force for the technologically advanced society we live in today [9]. To quit generating heat and electricity out of burning coal is still an ongoing discussion all around the world and might not be accomplished in the next couple of years. Graphite and diamond are widely known allotropes of carbon and could not be more different. This is due to different chemical hybridization of the carbon atom, as it can be sp^3 -hybridized and sp^2 - hybridized, in diamond and graphite, respectively. In graphite, the carbon atoms are covalently bonded resulting in a 2D hexagonal lattice and form a individual 2D material, known as graphene. The staking of an infinite number of sheets in a periodic manner, held together by weak van der Waals forces, lead to the structure of graphite. Graphene exhibits unique electronic properties and can also be rolled up to form carbon nanotubes (CNT) or upon implementation of pentagons instead of hexagons also form buckyballs know as fullerenes. As interesting as they are, a detailed description of their appearances and properties would go beyond the scope of this work, but can be found elsewhere [30–32]. Another form of carbon are activated carbons. They are widely used for different applications, such as electrode material for lithium-ion batteries, supercapacitors, water filters, water desalination and hydrogen storage. Activated carbons can be produced from various precursors, most interestingly biological waste materials via carbonization and activation processes. They are already produced from coconut shells, tea leaves, coffee beans, palm trees, bamboo, nut shells and many more [33]. Physical activation can be usually achieved by steam or CO_2 , while in chemical activation the precursors are impregnated with the activating reagent and are subsequently heated under an inert gas atmosphere, as shown exemplarily in Fig. 3.1 for the materials used in this work. A combination of both activation processes are also widely used. These activations result in the porous structure of these materials. As already mentioned, these pores can have different shapes, usually cylindrical and slit-like

shapes. The latter can be represented as two parallel graphene sheets separated by a distance equal to the pore width. A single graphene sheet exhibits a theoretical surface area of $1315 \text{ m}^2/\text{g}$ for each side [34]. The introduction of defects, such as replacing hexagons with hepta- and pentagons, can lead to buckling of the graphene sheets which enlarges the available surface area [35]. Distortions of the perfect stacking order of graphite, e.g. rotational distortions or buckling, are mostly present in activated carbons and the structure is referred to as turbostratic carbon. A visual representation of such a structure is given in Fig. 2.8 [34]. This kind of structure and the presence of defects is also revealed in experiments, such as X-ray diffraction and Raman spectroscopy. Both methods can be used to extract sizes above which correlation in lateral or axial direction is lost, denoted L_a and L_c , respectively [36,37].

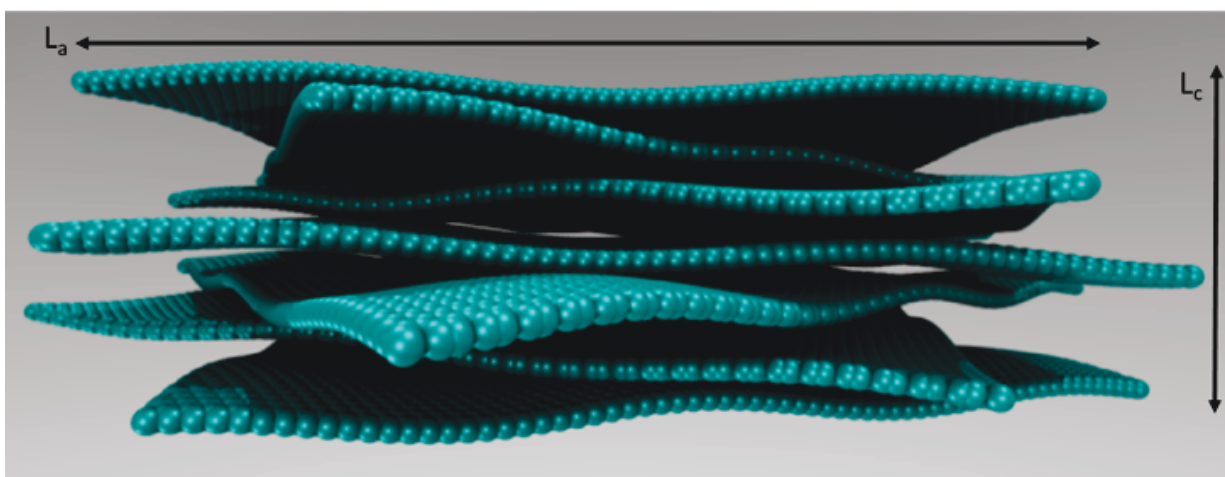


Fig. 2.8: Visualization of the turbostratic carbon structure. Adapted from Ref. [34] and with permission from American Chemical Society.

Raman spectroscopy is a technique which can determine vibrational modes of solid materials or molecules. The interaction of light with matter can be of elastic (like in X-ray scattering see section 2.3) or inelastic nature. In the case of inelastic Raman scattering, the scattered photons can possess either a lower (Stokes scattering) or a higher (anti-Stokes scattering) energy compared to the incoming photon. The change in energy originates from either the annihilation or creation of a phonon, and this energy (or

wavelength) shift is usually presented as the so-called Raman-shift in units of cm^{-1} and can be calculated with equation (2.8).

$$\Delta\bar{\nu} = \left(\frac{1}{\lambda_0} - \frac{1}{\lambda_1} \right) \quad (2.8)$$

Here λ_0 and λ_1 denote the wavelength of the incoming and the scattered photon, respectively. Theoretical works showed that it is possible to distinguish between single-layer or multi-layer graphene and turbostratic carbons. The Raman spectra of activated carbons consist of a characteristic D, G, D' and 2D (often labeled as G') mode bands [36,38]. The D-modes are in fact defect-activated and are not present in a perfect graphene structure, whereas the G-mode originates from in-plane stretching of the sp^2 -bonds. Such a Raman spectra of activated carbons is shown in Fig. 2.9.

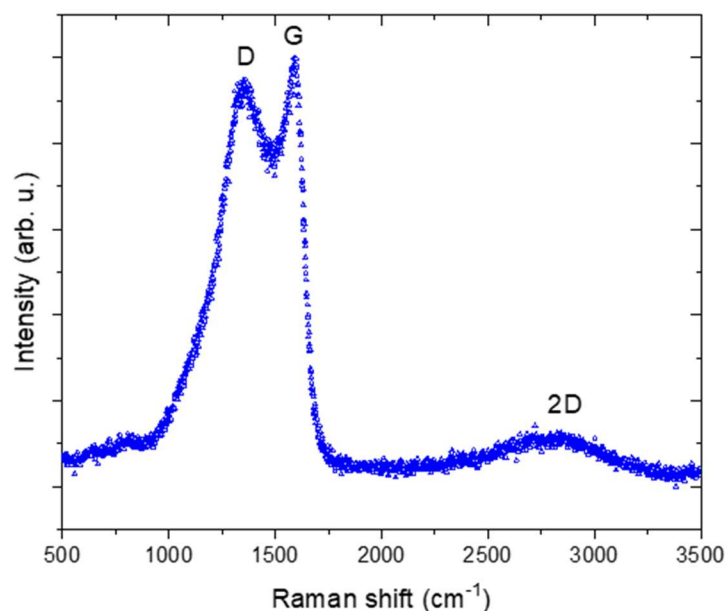


Fig. 2.9: Representation of a Raman spectra obtained from an activated carbon investigated in this thesis. A detailed evaluation of the band shapes and positions are given in section 4.

2.2.3 Hydrogen storage in nanoporous activated carbons

Hydrogen is usually stored in nanoporous carbons using cryogenic temperatures (< 100 K) and pressures up to 100 bar. At these conditions, H_2 is not behaving as an ideal gas and has to be treated as a supercritical gas. Therefore, the ideal gas law $P \cdot V_m = R \cdot T$ is not applicable as it assumes that intermolecular interactions are negligible compared to the thermal energy. Real gases are well described by the van der Waals (vdW) equation (2.9).

$$\left(P + \frac{a}{V_m^2}\right)(V_m - b) = RT \quad (2.9)$$

The constant a is a correction term to account for intermolecular attractive interaction forces, whereas the repulsion interactions are included in the volume b . These parameters are inherent to each gas. This equation of states (EOS) simplifies to the ideal gas law at high temperatures and large molar volumes. If the temperature decreases, an inflection point appears in the PV relation, which is at the critical temperature T_c . The pressure and the volume associated with this point are called critical pressure P_c and critical volume V_c , respectively. These critical values are derived from the vdW-EOS by zeroing the first and second derivatives of pressure with respect to molar volume and are found in good agreement with experimentally observed critical values, as shown in Fig. 2.1 [23]. As discussed earlier, the adsorption potential (Lennard-Jones-potential) is derived from the vdW-EOS and the net sum potential of the individual carbon atoms with the hydrogen molecules strongly depends on the confinement of the adsorptive gas inside the pore (Fig. 2.10). If the pore walls (assuming a slit-like shape) are getting closer to each other the sum potentials may overlap, resulting in a deep potential well, as shown in Fig. 2.10c [7,23,26].

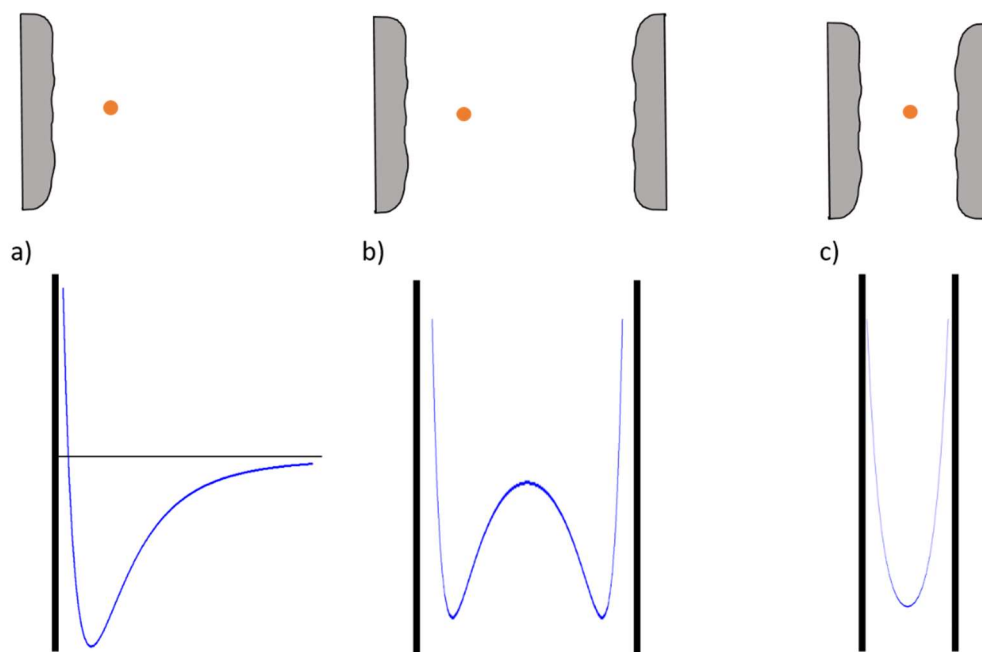


Fig. 2.10: Schematic illustration of the adsorption potential on a) a planar surface (macropore), b) a mesopore and c) a micropore. Adapted from Ref. [26]

In such a scenario the gas molecules are highly densified and the pressure inside the pores is multiple times higher than the applied external pressure [39]. At these conditions many-body interactions are gaining importance and equation (2.9) cannot fully describe the gas state. The virial equation offers a solution and is defined as:

$$Z = \frac{PV_m}{RT} = 1 + B_{(T)} + C_{(T)}P^2 + D_{(T)}P^3 + \dots = \alpha_{(T)} \cdot P + 1 \quad (2.10)$$

In this equation, B, C and D are the first, second and third virial coefficients, whereas α is the temperature depended non-ideality factor [7,23]. The virial equation may also be displayed as equation (2.11) and is used to fit experimentally observed isotherms, whereas n is the amount of hydrogen molecules adsorbed given in mol [40].

$$\ln P = \ln n + \frac{1}{T} \sum_{i=0}^m a_i n^i + \sum_{i=0}^m b_i n^i \quad (2.11)$$

These equations are formally used to describe the gas in its bulk state at low pressures and high pressures. There are many different Type I isotherm equations reported in the literature, some of fundamental and some of empirical nature [41]. One of the earliest derived isotherm equations is the so-called Langmuir equation, which calculates the surface coverage of adsorbed molecules as a function of pressure, assuming an energetically homogenous surface.

$$\Theta_A = \frac{bP}{1 + bP} \text{ and } b = b_0 \exp\left(-\frac{H_{ads}}{RT}\right) \quad (2.12)$$

Here, Θ_A is the fractional occupancy, the factor b is the affinity parameter, which is linked to the enthalpy of adsorption, whereas b_0 is related to the entropy of adsorption. Considering the heterogeneity of a surface, the surface coverage can be modeled by the generalized Freundlich-Langmuir equation:

$$n = \frac{a \cdot b \cdot P^c}{1 + bP^c}, \quad (2.13)$$

where b is the affinity constant, c the heterogeneity exponent and a is the maximal loading. If isotherms are collected at different temperatures, one can calculate the isosteric enthalpy of adsorption via the Clausius-Clapeyron equation (2.14) and fit the experimentally observed isotherm with the virial equation or any other Type I equation (corresponding to the Type I shape of the isotherm seen in Fig. 2.7):

$$\Delta H_{ads} = R \cdot \left[\frac{\partial \ln(P)}{\partial \left(\frac{1}{T}\right)} \right]_{\Theta} \quad (2.14)$$

The fitting procedure of the isotherms and application of the Clausius-Clapeyron equation to calculate the isosteric enthalpy is shown in section 4.4.2. Reported values for the isosteric enthalpy of hydrogen adsorption in nanoporous carbons range from 1-10 kJ/mol [7]. As illustrated in Fig. 2.10, the net sum adsorption potential depends on the

pore size and therefore also the pore specific enthalpy of adsorption. Generally, it is not possible to discriminate the pressure contributions to the overall pressure of different pore sizes from gas adsorption isotherms alone. Density Functional Theory (DFT), Grand Canonical Monte Carlo (GCMC) simulations and in-situ scattering experiments can help to understand these contributions [42–46]. The latter can give an estimate of the density of hydrogen in different pore sizes (Fig. 2.11a), whereas simulation methods can give an idea about the density profile within the pore (Fig. 2.11b).

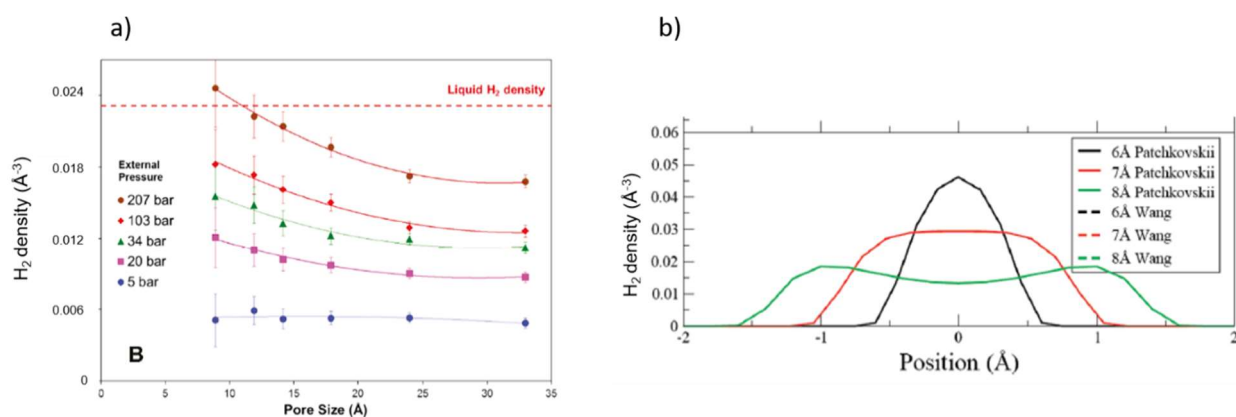


Fig. 2.11: a) H₂ density as a function of pore size at different pressures obtained at room temperature measured by in-situ Small Angle Neutron Scattering (SANS), adapted from Ref. [42] and b) H₂ density profile in different pore sizes; adapted from Ref. [39]. Both with permission from American Chemical Society.

2.3 Interaction of X-rays with matter

As briefly mentioned in the previous section, probing the material of interest with photons or neutrons can help to understand the porous structure. Small-Angle X-ray scattering (SAXS) and Wide-Angle X-ray scattering (WAXS) are useful techniques to investigate different size regimes. If an incident X-ray photon hits a material, different interactions can occur, as shown in Fig. 2.12. The intensity of the transmitted beam is lower compared to the incident beam, due to absorption of the photon's energy by the electrons (photoelectric effect).

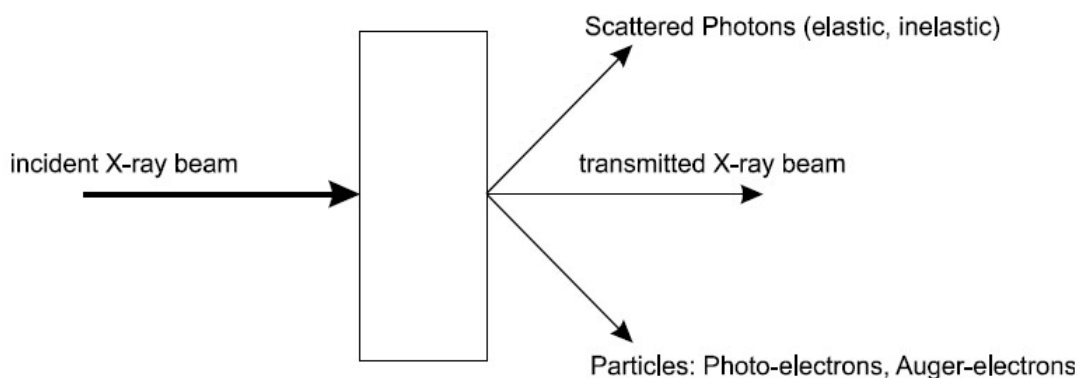


Fig. 2.12: Interaction of light with matter. Reproduced with permission from Ref. [47]

Inelastic scattering involves an energy transfer to (from) an electron from (to) the incoming photon. Therefore, the inelastically scattered photon has a different energy. The scattered wave has no fixed phase relation to the incoming wave, resulting in a constant intensity contribution, called incoherent background. Elastic scattering, on the other hand, gives rise to a fixed phase relation, which can be displayed at different levels, according to Fig. 2.13. The incoming wave with wavevector \vec{k}_1 is related to the scattered wave \vec{k}_2 by the scattering vector \vec{Q} via $\hbar\vec{Q} = \hbar(\vec{k}_2 - \vec{k}_1)$, where \hbar is the reduced Planck constant. Considering the wave nature and elastic scattering $|\vec{k}_2| = |\vec{k}_1| = \frac{2\pi}{\lambda}$, where λ is

the wavelength, the scattering vector is related to the scattering angle Θ via equation (2.15).

$$|\vec{Q}| = Q = \frac{4\pi}{\lambda} \sin(\Theta) \quad (2.15)$$

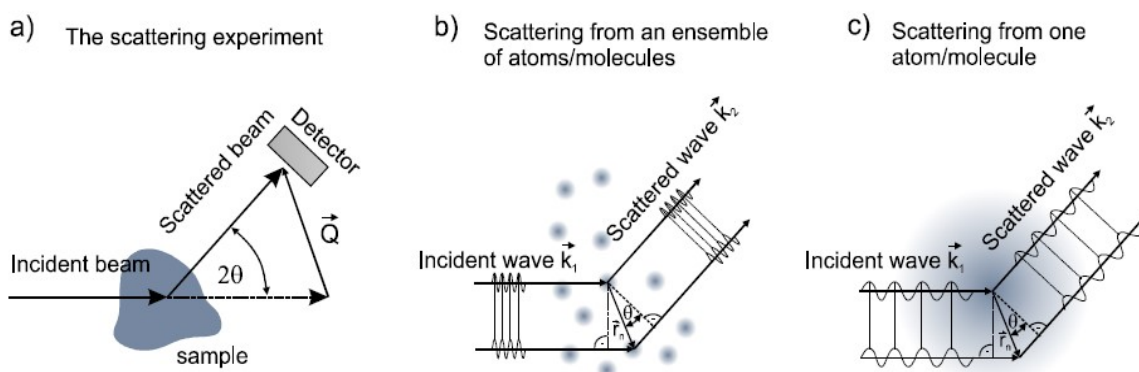


Fig. 2.13: Elastic coherent scattering process visualized at three different levels of magnification. Reproduced with permission from Ref. [47]

2.3.1 Small-angle X-ray scattering on nanoporous carbons

The theoretical background of SAXS on particulate systems is extensively discussed in literature [48,49] and the following section is a brief description of this method when applied to isotropic non-particulate as shown in Fig. 2.14. The measured and spherically averaged SAXS intensity as a function of the scattering vector of an ideal two-phase system consisting of pores (phase 1) and a carbon matrix (phase 2) is written in the form of:

$$I(Q) = V(1 - \varphi)\varphi(\Delta\rho)^2 \int_0^\infty 4\pi r^2 \gamma_0(r) \frac{\sin(Qr)}{Qr} dr, \quad (2.16)$$

where V is the irradiated volume, φ is the porosity (volume fraction of pores), $(\Delta\rho)^2$ is the scattering contrast ($\Delta\rho$ is the electron density difference) and $\gamma_0(\mathbf{r})$ is the normalized correlation function [3,47,49].



Fig. 2.14: Schematic representation of an isotropic two-phase system.

This relation holds as long as there are no correlations between the two-phase system and the atomic structure, e.g. the typical length scales are different. Debye, Anderson and Brumberger (DAB) introduced a simple analytical model to describe the scattering intensity of randomly shaped pore structures, by assuming an exponentially decaying correlation function [50].

$$\gamma_0(r) = \exp\left(-\frac{r}{a}\right) \quad \text{with } a = \frac{4V\varphi(1-\varphi)}{S} \quad (2.17)$$

Here, a is denoted as the correlation length (often Debye length) and is defined as the arithmetic average of the correlation function. S denotes the surface and V the irradiated volume. The scattering intensity in the analytical form thus reads:

$$I_{DAB}(Q) = \frac{2\pi(\Delta\rho)^2 \cdot S}{\left(\frac{1}{a^2} + Q^2\right)^2 \cdot V} \approx \frac{G}{\left(\frac{1}{a^2} + Q^2\right)^2} \quad (2.18)$$

If the absolute intensity is not experimentally available, the constants could be condensed into a single scaling parameter without physical meaning, as shown in the rightmost expression in equation (2.18).

In the limit of large scattering vectors ($Q \rightarrow \infty$), the scattering intensity of an ideal two-phase system with sharp interfaces decays according to Porod's law [49]:

$$I(Q \rightarrow \infty) = V \cdot (1 - \varphi)\varphi(\Delta\rho)^2 \cdot \frac{8\pi}{a} \cdot \frac{1}{Q^4} = (\Delta\rho)^2 \cdot \frac{2\pi}{Q^4} \cdot S = \frac{P}{Q^4} \quad (2.19)$$

The Porod constant P is related to the sample surface area S and can in general be extracted by plotting the measured scattering intensity multiplied by the fourth power of the scattering vector versus the fourth power of the scattering vector ($I(Q) \cdot Q^4$ vs. Q^4) [34,48]. Another general parameter, which does not depend on the structural features of the pores, is the integrated intensity (often mentioned as invariant) and can be calculated by:

$$\tilde{I} = \int_0^\infty I(Q) \cdot Q^2 dQ = 2\pi^2\varphi(1 - \varphi)(\Delta\rho)^2V \quad (2.20)$$

Combining equations (2.19) and (2.20) leads to equation (2.21), which can be rearranged to calculate the volume specific surface area as shown in equation (2.22).

$$\frac{\tilde{I}}{P} = \frac{2\pi^2\varphi(1 - \varphi)(\Delta\rho)^2V}{2\pi(\Delta\rho)^2S} = \pi\varphi(1 - \varphi)\frac{V}{S} \quad (2.21)$$

$$\frac{S}{V} = \pi\varphi(1 - \varphi)\frac{P}{\tilde{I}} \quad (2.22)$$

Nanoporous carbons mostly show a deviation from this ideal behavior (Q^{-4}) as they are not exhibiting sharp interfaces between the carbon matrix and the pore volume. These deviations might be explained from different views. Firstly, they could originate from a surface or mass fractal (rough surfaces of pores ~ 0.5 nm), which gives an exponent between -2 and -4 [49,51]. Secondly, they may arise from a smooth electron density transition between the pore and the matrix, which will influence the scattering intensity at large Q values [47,51]. According to Ruland, 1D density fluctuations within the solid

phase lead to an additive term proportional to Q^{-2} [52]. These fluctuations were found in turbostratic carbons and are attributed to fluctuations in the graphene interlayer distance. If those density fluctuations would be of random and isotropic nature and not in correlation with the pore structure, they would contribute to a constant background. In the picture of fluctuations of the interlayer spacing, the scattering intensity can be approximated:

$$I(Q) = I_{pore}(Q) + I_{fluct}(Q) + I_{Bg}(Q), \quad (2.23)$$

where I_{fluct} can be rendered as equation (2.24), according to Jafta et al. [53]:

$$I_{fluct}(Q) = \frac{Bl^2(18 + l^2Q^2)}{(9 + l^2Q^2)^2} \quad (2.24)$$

The parameter B scales the contribution of the fluctuations and the length l describes the size above which the lateral correlation in the carbon layers is lost, which could be similar to L_a obtained from XRD [53–55].

For large values of Q ($Q \cdot l \gg 1$) equation (2.24) decays proportional to Q^{-2} and together with the most right side of equation (2.19) leads to a modified Porod law:

$$I(Q) = \frac{P}{Q^4} + \frac{B}{Q^2} + C \quad (2.25)$$

The fluctuation contributions have to be subtracted from the measured SAXS intensity in order to treat it as an ideal two-phase system and to correctly apply the aforementioned equations. In the literature, two main approaches can be found and both provide valid insights for the different views of the origin of the fluctuations. Firstly, Wang et al. treated the fluctuations as a constant background and obtained the parameter B together with the Porod constant P from plotting $I(Q) \cdot Q^4$ vs. Q^4 and linear fitting in the high Q regime [34]. The integrated intensity was then calculated by $\tilde{I} = \int_{d_{min}}^{\infty} [I(Q) - B] \cdot Q^2 dQ$ and together with equation (2.22) they calculated the ratio

S/V . Prehal et al. uses a similar approach, but obtains the constant contribution by a power law in the form of $A \cdot Q^{-\alpha} + C$ at large scattering vectors and subtracts just the constant background [47,56,57].

Jafta and coworkers used the first two terms on the right side of equation (2.25) and derived B and P by plotting $I(Q) \cdot Q^4$ vs. Q^2 and linear fitting in the high Q regime [53]. They then used equation (2.24) and subtracted this contribution from the measured SAXS intensity, choosing l in such a way that I_{fluct} did not exceed the measured intensity but appropriately fit at large scattering vectors. Koczwara et al. directly fitted equation (2.25) in the high Q regime and set l as L_a (obtained from X-ray diffraction data) and subtracted this contribution together with C from the measured intensity [55]. Another approach was used by Santos et al., as they obtained B similar to Jafta et al., but just subtracted $B \cdot Q^{-2}$ from the measured intensity [58].

After arriving at the intensity of the two-phase system, regardless of the approach used, the SAXS signal can be further analyzed to calculate some structural properties. The Porod length t or average chord-length can be obtained by dividing the integrated intensity by the Porod constant, which is correlated to the average chord length of the pores $\langle l_{pore} \rangle$ and of the carbon matrix $\langle l_{carbon} \rangle$ according to equation (2.26), as follows:

$$t = \frac{4\tilde{I}}{\pi P} = (1 - \varphi)\langle l_{pore} \rangle = \varphi\langle l_{carbon} \rangle = \frac{4V\varphi(1 - \varphi)}{S} \quad (2.26)$$

Generally, a chord is the length between two points on the surface of a structure, where the scattering contrast along the line is constant, e.g. inside the carbon matrix or the pore space as shown in Fig. 2.15.

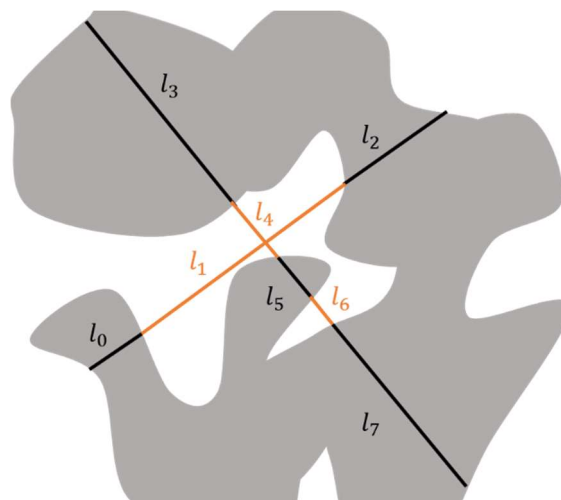


Fig. 2.15: Schematic representation of the chord length in a two-phase system. Black lines indicate carbon matrix and orange lines the pore space (own work).

2.3.2 Wide-angle X-ray scattering on nanoporous carbons

Measuring the scattering intensity at higher angles Θ (or scattering vectors) results in probing distances in the size regime of crystal lattice distances. A crystal lattice exhibits a periodicity, which allows for certain angles of two scattered X-ray beams to interfere constructively, leading to a measurable intensity signal (see Fig. 2.16).

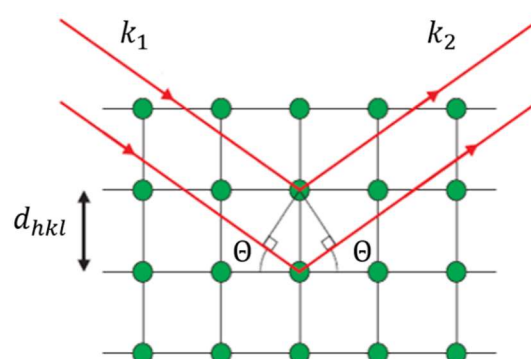


Fig. 2.16: Scattering on a periodic lattice. The distance between two crystal planes is denoted as d_{hkl} . The wavevectors k_1 and k_2 denote the incoming and the reflected waves, respectively. Adapted from Ref. [48] with permission from John Wiley and Sons.

The relation for constructive interference is given by equation (2.27), which is known as Bragg's law. Here, hkl denote the so-called Miller indices from the reciprocal lattice, which indicate different crystal lattice planes.

$$d_{hkl} = \frac{\lambda}{2 \cdot \sin(\Theta_{hkl})} = \frac{2\pi}{Q_{hkl}} \quad (2.27)$$

A schematic representation of the perfect graphite crystal lattice is shown in Fig. 2.17. Deviations from perfect periodicity, such as differences in the stacking height of the graphene sheets or the implementation of defects, can alter the peak positions and the peak width [37].

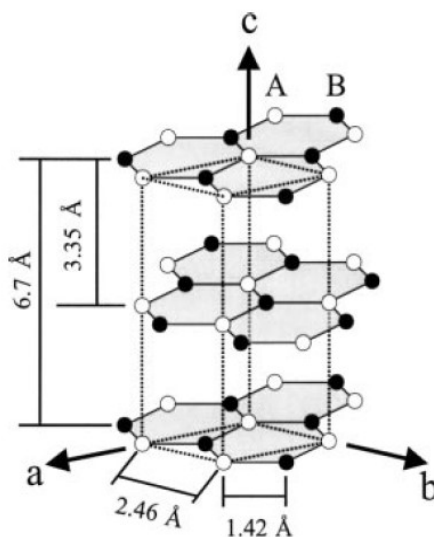


Fig. 2.17: Schematic representation of the graphite crystal lattice. a,b and c denote the real space axis. The stacking order of the graphene hexagons results in a difference in the carbon atoms, A and B. The distance between two neighboring A-carbon atoms is 1.42 Å, for A-and B-atoms it is 2.46 Å and the distance between two graphene layers is 3.35 Å. Reprinted from Ref. [59].

Measuring the Full Width at Half Maximum (FWHM) in nm^{-1} of a certain Bragg peak gives rise to the correlation length in a certain $[hkl]$ -direction, e.g. the length of perfect crystallinity. The parameter L_a is denoted as correlation length within the graphene

sheet (in-plane size of the sheets), whereas L_c measures the stacking correlation or the stacking height [55,60,61]:

$$L_a = 1.84 \cdot \frac{2\pi}{FWHM_{(10)}} \text{ and } L_c = 0.91 \cdot \frac{2\pi}{FWHM_{(002)}} \quad (2.28)$$

Different peak shapes could also reveal the underlying stacking structure but a detailed evaluation requires sophisticated measurements and is usually hard to obtain in turbostratic carbon [62,63].

3 Experimental methods

3.1 Carbon materials and synthesis

The biomass-derived activated carbon materials were synthesized and provided by collaborators from the Institute of Bioproducts and Paper Technology at Graz University of Technology (research group of Stefan Spirk). All three samples were synthesized following the protocol shown in Fig. 3.1. Waste materials were used as carbon precursors, namely spent coffee grounds, silver skins from coffee beans and fines from paper production.

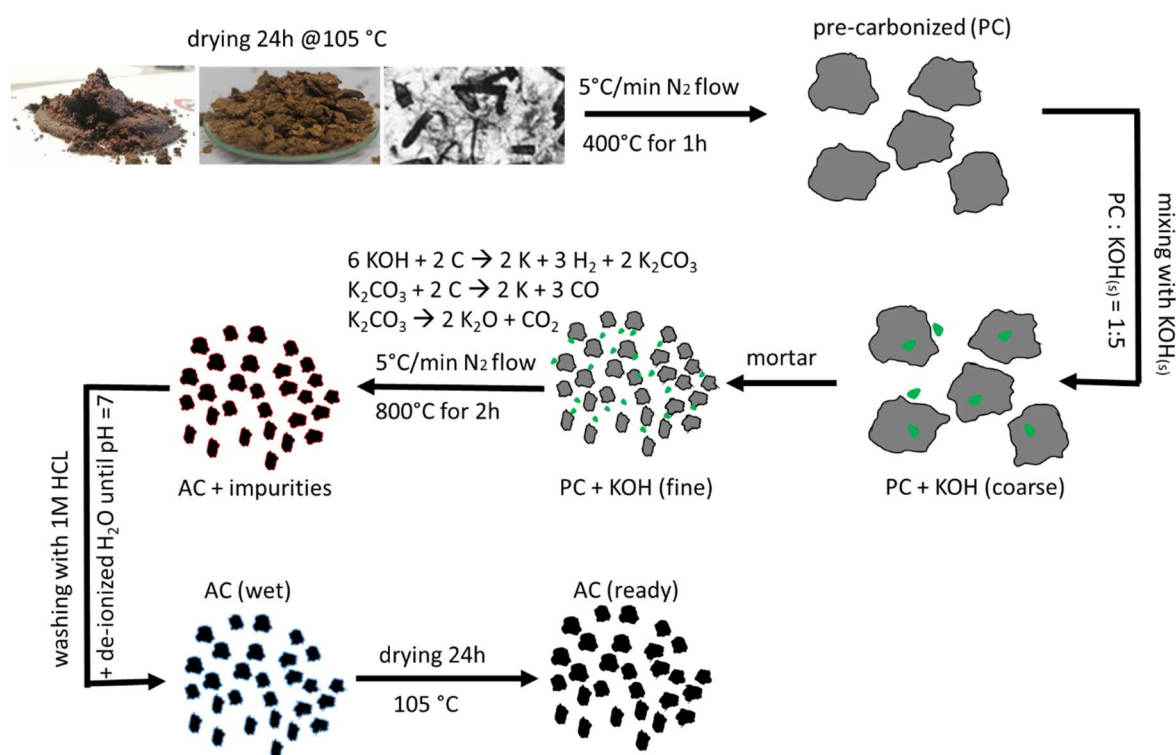


Fig. 3.1: Synthesis of activated carbon materials from bio-waste. Adapted with permission from Ref. [64].

The wet samples were dried at 105 °C for 24 h and then heated to 400 °C under nitrogen gas flow with a heating rate of 5 °C/min and were held at this temperature for 1 h. The pre-carbonized materials were then mixed with solid potassium hydroxide (KOH) in a mass ratio of 1:5. After grinding, the mixture was heated to 800 °C under nitrogen gas flow and was held for 2 h. At this temperature, the solid KOH reacts with the carbon and forms different reaction products, as displayed in Fig. 3.1. The chemical reactions

lead to a reduction in carbon mass and leave pores inside the materials. The now activated carbon materials still contain impurities, which are removed by washing with 1 M hydrochloric acid and de-ionized water until a pH-value of 7 is reached. After drying at 105 °C for 24 h, the materials were ready to be characterized by the following methods.

3.2 Materials characterization

3.2.1 Gas sorption analysis and hydrogen sorption experiments

Gas sorption experiments were performed with an Autosorb iQ3 gas sorption analyzer (Quantachrome/Anton Paar) using nitrogen (N_2), argon (Ar) and carbon dioxide (CO_2) gases of ultra-high (99.999 %) purity. The carbon materials were outgassed under vacuum (10^{-6} mbar) for 24 h at 250 °C before every measurement and the used sample mass was between 30-60 mg. The samples were placed in glass cells of different shapes (bulb or cylindrical), depending on the used external equipment. To reduce the cell volume glass filling rods were placed inside and the dead volume of the sample cell was automatically evaluated before each run using helium gas. N_2 adsorption/desorption isotherms were recorded at 77.3 K in a relative pressure range of P/P_0 from 10^{-6} to 0.99 in 77 steps for adsorption and 36 steps for desorption. Ar isotherms were recorded at 87.3 K using an external cryostat equipment (Cryosync) while similar number of steps were used as in the nitrogen experiments. Additionally, CO_2 isotherms were recorded at 273.15 K using a bath filled with a mixture of water and anti-freezing liquid which was coupled with an external temperature controlling device. In an absolute pressure range of $1.2 \cdot 10^{-3}$ and 1 bar, a total of 57 and 37 adsorption and desorption points, respectively, were recorded. The specific surface areas (SSA) were estimated by the multi-point Brunauer-Emmet-Teller (BET) method following the BET consistency criteria of the International Standard Organization (ISO 9277:2010) as well as by the Quenched Solid Density Functional Theory (QSDFT) method using the N_2 -carbon and Ar-carbon equilibrium transition kernels at 77 K and 87 K, respectively, for slit pores [26]. The total pore volume

(TPV) as well as the pore size distribution (PSD) was calculated using the QSDFT kernels for slit-pore geometries, which are implemented in the software provided by Quantachrome/Anton Paar [65]. For nitrogen and argon, these values were obtained using a QSDFT kernel while for carbon dioxide a GCMC kernel was used.

The hydrogen isotherms were recorded at 77, 87 and 97 K using the same sample for the different measurements. To further ensure consistency, the samples were degassed for 24 h at 250 °C ahead of a new experiment. For all measurements 57 adsorption and 20 desorption points in a pressure range of 10^{-3} -1000 mbar were recorded. To ensure a constant temperature the measurements were conducted similar to the aforementioned approaches. For the experiments at 77 K a liquid nitrogen bath was used, whereas for 87 and 97 K the external cryostat equipment (Cryosync) was used.

3.2.2 Raman spectroscopy

To record the Raman spectra, a confocal spectrometer, equipped with a frequency-doubled Nd-YAG laser emitting at 532.2 nm (Jobin-Yvon LABRAM), was used. The laser beam (power density of $0.1 \text{ mW}/\mu\text{m}^2$ and spatial resolution of 1.5 cm^{-1}) was focused on the sample by an Olympus BX 40 microscope fitted with an x50 long-working distance objective lens. The outgassed samples from the nitrogen gas sorption experiments were used to ensure that no contaminations were present. The fine powder samples were placed on a glass substrate and were smoothed to a uniform height using a spatula. Through probing different sample areas, the uniformity of the spectra could be verified and the spectra with the highest signal to noise ratio was used for analysis purposes.

3.2.3 X-ray Scattering

X-ray diffraction (XRD) experiments were performed with a D8 Advance Eco (Bruker AXS) instrument equipped with a Cu-K α X-ray sealed tube (40 kV, 25 mA, $\lambda=0.154$ nm) and an energy sensitive detector (LYNXEYE-XE). The recorded angular range (2θ) was set between 10 and 130° with a step size of 0.01° and an exposure time of 1 s/step. The measurements were performed on the previously degassed samples using a zero-background sample holder.

SAXS experiments were carried out with the laboratory SAXS instrument (NanoStar, Bruker AXS) using Cu-K α radiation from an X-ray microsource (45 kV and 0.650 mA) and a Vantec 2000 area detector. The sample chamber was held under vacuum at 0.1 mbar during the measurements to reduce air scattering. The measurements were conducted at three different sample-to-detector distances to cover a wide Q-range (25, 65 and 107 cm, which correlates to a scattering vector range between ~ 18 and ~ 0.05 nm⁻¹). Firstly, all samples were measured for 10 min and afterward the transmission signal was measured for another 10 min. In order to get an average scattering signal from different positions in the samples, measurements of 30 min were performed to increase the statistics. The previously degassed samples were filled in an aluminum sample holder with a hole of rectangular shape (0.5 mm x 2 mm) and were compressed with an axial pressure of 1 ton to form a free-standing pellet. For one sample, which was too fine-grained to be compressed, a specially designed precision sample holder was built (see Fig. 3.2), on which a pile of the degassed powder could be placed.

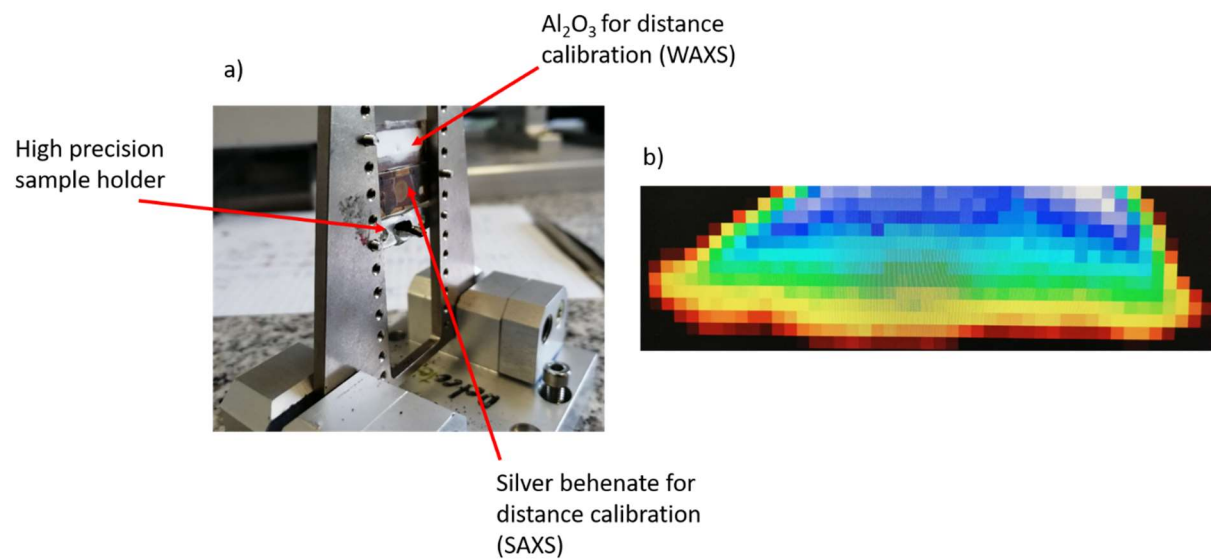


Fig. 3.2: a) sample holder with distance calibration standards and b) scan of the sample pile on the sample holder to evaluate good measurement positions.

The aforementioned efforts of sample preparation were required to reduce the background signal, particularly in the high- Q region, since subtraction of tape, which was frequently used to secure the powder in the sample holder in previous studies [3,47] can create severe difficulties due to its strong scattering signal. The obtained 2D scattering patterns were radially integrated using the MULIP software (provided by Gerhard Popovski from the Institute of Physics, Montanuniversität Leoben) and were transmission corrected [66].

4 Results and Discussion

In the following pages, the results obtained from the experiments explained in section 3 will be shown and discussed. For this purpose, the following nomenclature is implemented and will continue throughout this section. The samples investigated were activated carbons (AC) produced from fines out of paper production, silver skin from coffee beans and spent ground coffee, which are denoted as AC-Fs, AC-CSS and AC-SCG, respectively. A suitable color scheme for the presented data derived for these samples is also preserved in the graphs of this section. In particular, AC-Fs is shown by black triangles, AC-CSS by red circles and AC-SCG by blue squares. In the first sections the structural analysis of the materials is shown, whereas towards the end of this section the H_2 adsorption data will be presented and discussed with respect to the obtained structural parameters.

4.1 Structural parameters obtained by Raman spectroscopy

Raman spectroscopy is used as a versatile technique to investigate samples of various compositions and origin. Especially in carbon materials, such as graphite, graphene or turbostratic carbon, Raman spectroscopy was widely used to probe the nature of defects and the structure of these materials [67–70]. As shortly discussed in section 2.2.2, the Raman spectra of single-layer graphene, multi-layer graphene and turbostratic carbon differ in the appearance and relative intensity of certain bands in the spectra [36]. As shown in Fig. 4.1, the spectra exhibit three band peaks. The first one is associated with the D-band (not present in perfect graphene) around 1360 cm^{-1} , which arises from in-plane distortions, which may also be related to sp^3 -hybridization of carbon atoms [36,71]. The second one is called G-band around 1560 cm^{-1} , which results from in-plane stretching of the sp^2 -bonds. The broad peak at Raman shifts of $\sim 2870\text{ cm}^{-1}$ (approximately twice the frequency of the D-band) is called the 2D-band (or G'-band) originating from second-order scattering processes and is also found at the edges of single-layer graphene. The intensity ratio of the G-band and the D-band can be used to calculate the in-plane correlation length, which is related to the one calculated from XRD data, as shown in section 4.3.1. Matthews et al. proposed an empirical relationship between L_a and the ratio of the band intensities [69]:

$$L_a = (-12.6 \text{ nm} + 0.033 \cdot \lambda_{laser}) \cdot \left(\frac{I_G}{I_D}\right) \quad (4.1)$$

Here, λ_{laser} is the used laser wavelength (in nm), which was 532.2 nm for the presented experiments. However, literature does not clearly state how to obtain the ratio in equation (4.1). Some authors suggest to use the maximum value of the peaks, whereas others fit the spectra with different types of functions and they use the maximum value or the peak area [37,72]. Most commonly the D- and the 2D bands are fitted with a Lorentzian distribution function, whereas the G-band is fitted with either the symmetric Gaussian or Lorentzian distribution function or as well with the asymmetric Breit-Wigner-Fano (BWF) distribution as shown in Fig. 4.1a-c [36,73–75].

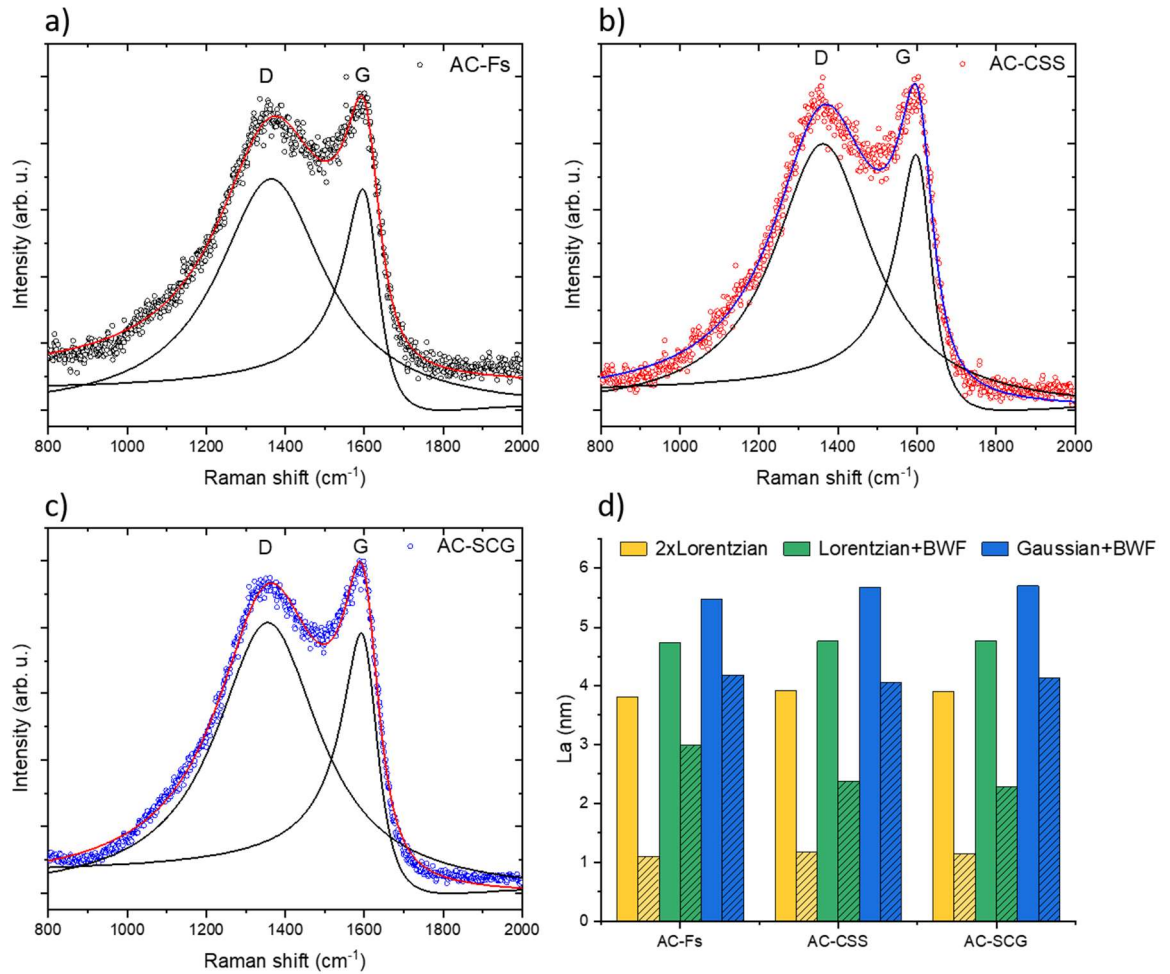


Fig. 4.1 a-c): Raman spectra of the different materials investigated in this thesis. Hollow symbols are the measured data, solid black curve below the D-band is a Lorentzian function, solid black curve below the G-band has a BWF-shape and the solid colored lines represent the sum fitting curve. d) shows a summary of L_a values obtained from the different fitting approaches: yellow represents fitting of the D- and G-band with Lorentzian functions, green the fitting with a Lorentzian and BWF function for the D- and G-band, respectively and blue represents the fitting with a Gaussian and BWF function. The full bars represent the band height ratio and the striped bars the area ratio.

The 2D-band is not shown in Fig. 4.1, but can be fitted with a single Lorentzian function, which reflects the turbostratic nature of the materials [36]. The different fit approaches result in very different outcomes for the in-plane correlation length L_a as summarized in

Table 4.1. The first approach of using two Lorentzian function to fit the D- and the G-band show the lowest values. The values calculated from the area ratio in the first approach are ~ 1.15 nm, due a very broad D-band fit and thus cannot be trusted as equation (4.1) is only valid above 2 nm [37].

Table 4.1: Values obtained for L_a with the different fitting approaches described above and in the caption of Fig. 4.1.

Material	Two Lorentzians		Lorentzian and BWF		Gaussian and BWF	
	L_a (nm)		L_a (nm)		L_a (nm)	
	Height ratio	Area ratio	Height ratio	Area ratio	Height ratio	Area ratio
AC-Fs	3.80	1.10	4.74	2.98	5.48	4.17
AC-CSS	3.92	1.17	4.77	2.37	5.67	4.05
AC-SCG	3.89	1.15	4.78	2.28	5.70	4.12

The Gaussian-shaped function for the D-band is equally valid as the Lorentzian-shape and the obtained L_a is around 1 nm higher as compared to the second approach. Furthermore, the fit was better for the combination of the Lorentzian shape and the BWF shaped function. In case of the height ratio, the values from second approach meet fairly well the mean between the other two approaches (4.77 compared to the mean of 4.80 nm for the AC-SCG) and thus strengthen the superiority of this fitting functions. Nevertheless, the individual values should be considered with caution and compared to similar values obtained from other methods.

4.2 Structural parameters obtained by gas sorption analysis

In the following pages, the structural parameters or pore characteristics obtained by gas adsorption using different gases will be shown. For clarity, in the summarizing tables some terms have to be specified. The d_{50} parameter represents the volume-weighted median of the pore sizes, whereas d_{25} and d_{75} denote the 25th and 75th percentile of the pore size, respectively [55]. Those values are estimated from the cumulative PSD shown in Fig. 4.2: Cumulative pore size distribution and indication of the volume-weighted median of the pore sizes and the corresponding 25th and 75th percentile.

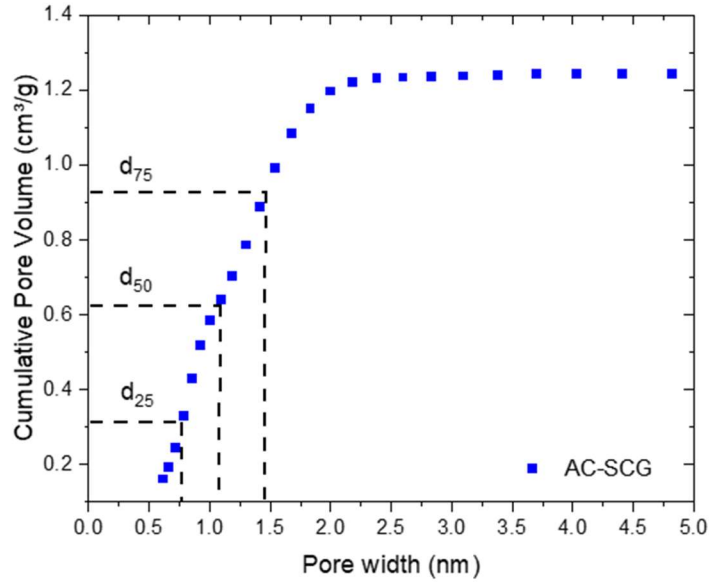


Fig. 4.2: Cumulative pore size distribution and indication of the volume-weighted median of the pore sizes and the corresponding 25th and 75th percentile.

The average pore width is calculated from the specific surface area and the specific pore volume obtained by the QSDFT kernel (for slit pores) as follows [7]:

$$\text{average pore width} = 2 \cdot \frac{V_{QSDFT-slit}}{S_{QSDFT-slit}} \quad (4.2)$$

In Fig. 4.3a the gas adsorption and desorption data of the different materials measured with N_2 at 77 K is shown. The AC-Fs sample shows the lowest nitrogen uptake, and the isotherm exhibits characteristics of type I and type IV isotherms according to IUPAC classification (see Fig. 2.7).

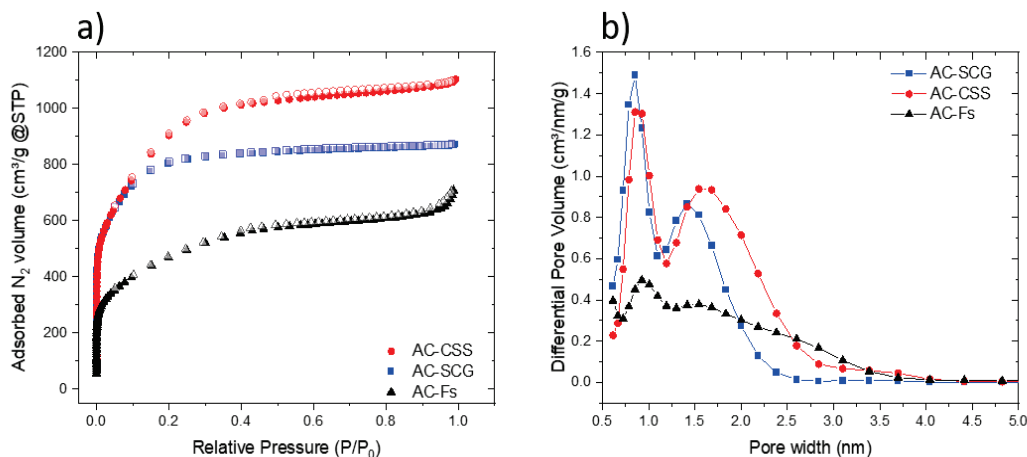


Fig. 4.3: a) N_2 gas sorption isotherms obtained at 77 K. Full symbols show adsorption data and hollow symbols show desorption data and b) PSD obtained by the QSDFT slit-pore model for carbons and N_2 .

At low relative pressures, the micropore filling takes place up to ~ 170 cm³/g. With increasing relative pressure, the adsorbed amount increases and a steep uptake at $P/P_0 \sim 0.99$ due to external surface adsorption or condensation of nitrogen in the macropores can be seen. The desorption branch shows a small deviation from the adsorption points, known as hysteresis loop, due to capillary condensation within the mesopores. The isotherms of the AC-SCG material and the AC-CSS material show a steep micropore filling up to ~ 500 cm³/g, which indicates a high micropore volume and is related to strong gas-solid interactions [24,26]. For the AC-SCG material, a saturation plateau is reached at around 860 cm³/g and the desorption branch shows no hysteresis. Therefore the isotherm is purely of type I based on the IUPAC classification. In the case of AC-CSS, a slow increase of the adsorbed amount at relative pressures beyond 0.01 is associated with filling of the wider micropores, where adsorbate-adsorbate interactions are

dominating. At $P/P_0 \sim 0.5$ a weak hysteresis loop is closing, which implies the presence of mesopores in which capillary condensation can occur and the maximum N_2 uptake of $1100 \text{ cm}^3/\text{g}$ was found at $P/P_0 \sim 0.99$. The small increase at higher relative pressures originates from some minor external surface. These characteristics of the isotherms are also reflected in the PSD plots shown in Fig. 4.3b, as the AC-CSS and AC-SCG materials exhibit a higher specific pore volume and SSA compared to the AC-Fs material. The smallest average pore width of around 1 nm was found for the AC-SCG material, but the highest nitrogen uptake occurs in the AC-CSS material with an average pore width of 1.22 nm. A summary of the porosity properties is given in Table 4.2.

Table 4.2: Summary of porosity properties obtained by N_2 gas adsorption at 77 K. (a) volume-weighted median of the pore sizes d_{50} and the corresponding 25th and 75th percentile (d_{25} and d_{75}), derived from the cumulative PSD plot (similar Fig. 4.2). (b) Average pore width calculated with equation (4.2).

Material	S_{BET} (m^2/g)	$S_{\text{QSDFT-Slit}}$ (m^2/g)	$V_{\text{QSDFT-Slit}}$ (cm^3/g)	$d_{50} (d_{25} - d_{75})^{(a)}$ (nm)	average pore width ^(b) (nm)
AC-Fs	1683	1466	0.97	1.58 (0.97-2.44)	1.32
AC-CSS	3308	2568	1.57	1.14 (0.93-1.53)	1.22
AC-SCG	2987	2529	1.24	0.96 (0.77-1.47)	0.99

The gas sorption isotherms obtained with Ar at 87 K, seen in Fig. 4.4a, demonstrate a similar trend as the isotherms obtained by N_2 . For the AC-Fs material no hysteresis loop can be seen, but also no clear saturation plateau was reached. The micropore filling in the AC-SCG material was a bit higher than for AC-CSS. However, the SSA obtained from QSDFT is also higher for the AC-SCG, whereas the BET-SSA is lower compared to AC-CSS. This reflects the limited applicability of the multi-point BET-method for microporous materials. The trend of the average pore width is also seen in the PSD shown in Fig. 4.4b.

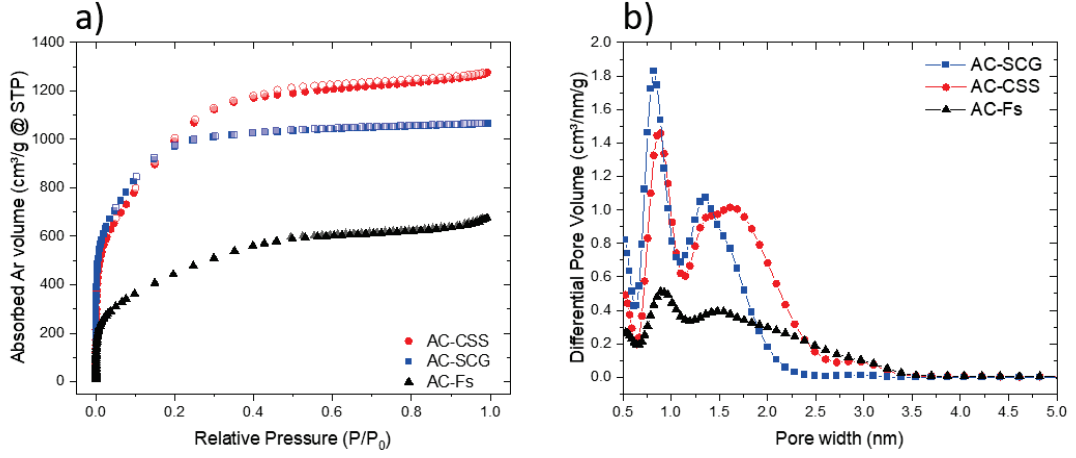


Fig. 4.4: a) Ar gas sorption isotherms obtained at 87 K. Full symbols show adsorption data and hollow symbols show desorption data and b) PSD obtained by the QSDFT slit-pore model for carbons and Ar.

While the PSD for the AC-Fs is very similar to the one obtained by N_2 , for the other two materials it shows an increase below a pore width of 0.6 nm, which hints to even smaller pores. The peak in the PSD of AC-CSS at around 1.75 nm in Fig. 4.3b is better resolved in Fig. 4.4b. A summary of the pore properties obtained by Ar gas sorption is given in Table 4.3. The slow kinetics of gas diffusion at cryogenic temperatures as in the case of N_2 and Ar lead to restrictions for the characterization of very narrow micropores [24]. Therefore, the use of CO_2 at 273 K as the adsorptive gas at low pressures helps to address this problem, as the kinetic diameter (0.33 nm) is a bit smaller than those of N_2 and Ar (0.36 nm and 0.34 nm, respectively) [76].

Table 4.3: Summary of porosity properties obtained by Ar gas adsorption at 87 K. (a) volume-weighted median of the pore sizes d_{50} and the corresponding 25th and 75th percentile (d_{25} and d_{75}), derived from the cumulative PSD plot (similar to Fig. 4.2). (b) Average pore width calculated with equation (4.2)

Material	S_{BET} (m^2/g)	$S_{QSDFT-Slit}$ (m^2/g)	$V_{QSDFT-Slit}$ (cm^3/g)	d_{50} ($d_{25} - d_{75}$) ^(a) (nm)	average pore width ^(b) (nm)
AC-Fs	1443	1211	0.82	1.58 (1.02-2.26)	1.36
AC-CSS	3261	2552	1.57	1.42 (0.94-1.81)	1.23
AC-SCG	3142	2646	1.31	1.09 (0.79 -1.43)	0.99

The CO₂ gas sorption isotherms (Fig. 4.5a) are usually presented with the uptake in mmol/g units versus the absolute pressure in mbar units, since experimentally used pressures are far below the saturation vapor pressure of ~35 bar. To convert the uptake from cm³/g, equation (4.3) is used, where V_m is the molar volume at STP conditions.

$$\text{uptake} \left(\frac{\text{mmol}}{\text{g}} \right) = \frac{\text{uptake} \left(\frac{\text{cm}^3}{\text{g}} \right)}{V_m \left(\frac{\text{cm}^3}{\text{mol}} \right)} \cdot 10^3 \text{ with } V_m = 22.414 \cdot 10^6 \left(\frac{\text{cm}^3}{\text{mol}} \right) \quad (4.3)$$

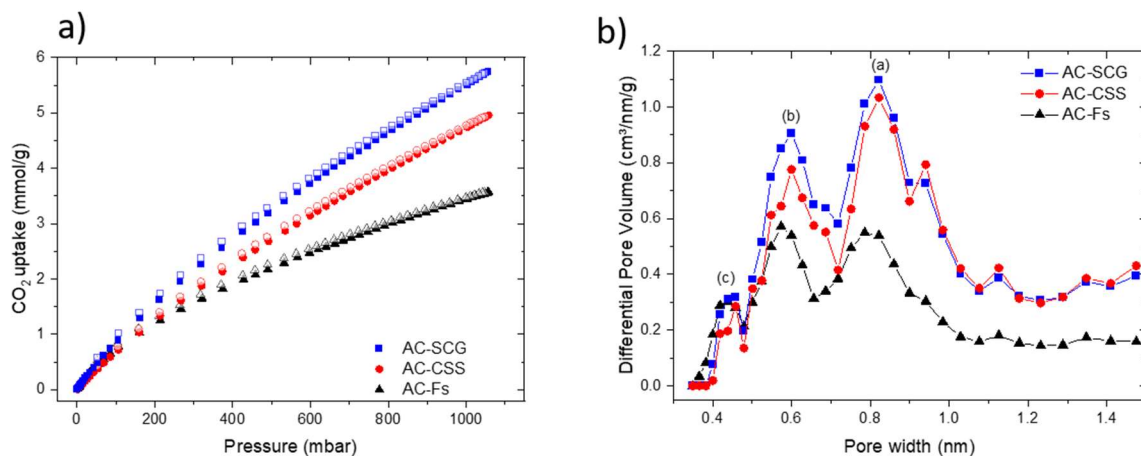


Fig. 4.5: a) CO₂ gas sorption isotherm obtained at 273 K. Full symbols show adsorption data and hollow symbols show desorption data and b) PSD obtained by the GCMC slit-pore model for carbons and CO₂. The insets (a), (b) and (c) mark the peak positions and can be found in Table 4.4.

The CO₂ gas sorption isotherms by themselves do not reveal or relate to any structural details, but the PSD analysis (see Fig. 4.5b) using the GCMC simulation kernel for slit pores show a continuation of the PSDs obtained by N₂ and Ar. The sharp peaks seen in Fig. 4.3b and Fig. 4.4b around 0.8 nm are also displayed in the PSD obtained by CO₂. Furthermore, peaks are found at pore widths around 0.6 and 0.45 nm, whereas the latter may relate to a smaller percentage to the absolute pore volume. A summary of the pore widths at the peak positions is given in Table 4.4.

Nevertheless, the CO₂ “storage” capability may be addressed at this point. The AC-SCG material exhibits the highest uptake of 5.7 mmol/g at 273 K and ~1 bar, whereas an uptake of 4.95 and 3.67 mmol/g is found for AC-CSS and AC-Fs, respectively.

Table 4.4: Summary of pore sizes obtained from the maxima positions in PSD calculated from CO₂ gas adsorption isotherms using a GCMC slit-pore kernel. (a), (b) and (c) correspond to the peak positions in Fig. 4.5b.

Material	Pore size ^(a) (nm)	$V_{pore}^{(a)}$ (cm ³ /g)	Pore size ^(b) (nm)	$V_{pore}^{(b)}$ (cm ³ /g)	Pore size ^(c) (nm)	$V_{pore}^{(c)}$ (cm ³ /g)
AC-Fs	0.80	0.17	0.57	0.07	0.44	0.02
AC-CSS	0.82	0.24	0.60	0.08	0.46	0.01
AC-SCG	0.82	0.29	0.60	0.11	0.46	0.02

4.3 Structural parameters obtained by X-ray scattering

4.3.1 Wide angle X-ray scattering

The WAXS patterns are shown in Fig. 4.6a and b, whereas the measurements were conducted in air and in vacuum, respectively. The pattern of AC-Fs reveals the characteristic peaks for graphitic carbons around 15 and 30 nm⁻¹ corresponding to the (002)-stacking and the (10)-in-plane reflections. Both peaks are broad, which is attributed to low (or short-range) order in those directions. The stacking peak cannot be observed in the diffraction patterns of the AC-CSS and AC-SCG materials, due to air scattering. The background of the peaks were fitted using a straight line in the double logarithmic plot (corresponding to a power law) and this contribution was subtracted from the diffraction pattern to isolate the peak. Afterwards, the peaks were fitted using a Gaussian function and with equation (2.28), it is possible to calculate the correlation lengths L_a and L_c , and from the peak positions the lattice parameters a and c can be obtained.

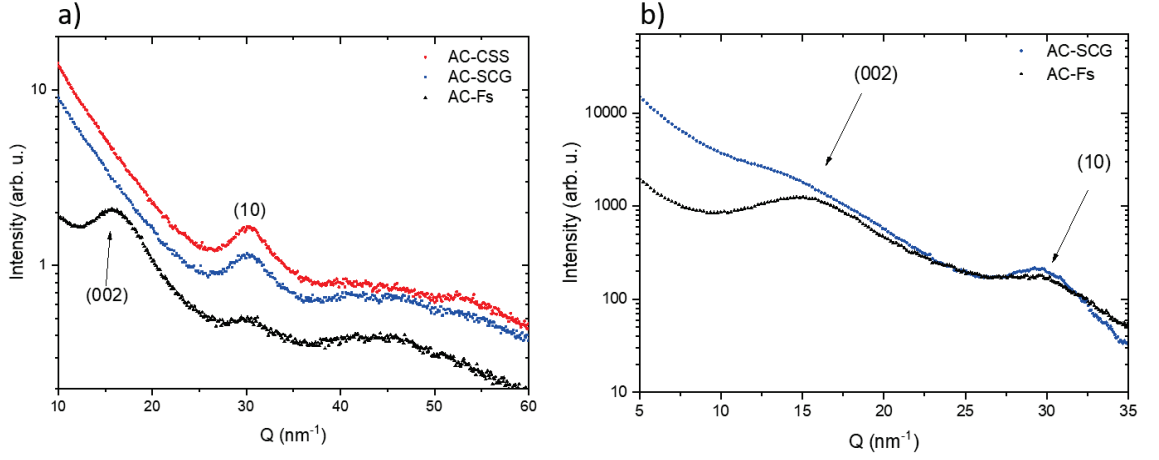


Fig. 4.6: a) WAXS pattern of the different materials with indication of the (002) stacking peak and the (10) in-plane peak measured in air and b) WAXS pattern of AC-SCG and AC-Fs, also with indication of the peak positions measured in vacuum. AC-CSS could not be measured, due to unlucky events during evacuation of the sample chamber and due to an insufficient amount of sample material.

The lattice parameter of the graphene layer can be calculated using the formula $a = \frac{2 d_{hk}}{\sqrt{3}} (h^2 + k^2 + hk)$, where h and k are the Miller indices. For all ACs, a was calculated to be ~ 0.239 nm, which is slightly smaller than the lattice parameter of a perfect graphene layer (0.2466 nm). The in-plane correlation length resulted in 3.20, 2.90 and 2.82 for the AC-Fs, AC-CSS and AC-SCG materials, respectively. The obtained values are in a similar range and follow the same trend compared to the ones obtained from Raman spectroscopy using the fitting procedure with a Lorentzian shaped and a BWF shaped function for the D- and G-band, respectively. The stacking correlation length was calculated for the AC-Fs and resulted in 1.03 nm, which correlates with the layer distance $c/2$ of 0.396 nm, to about four stacked graphene layers (using $n = 2 \cdot \frac{L_c}{c} + 1$). For the AC-SCG L_c was found to be 0.63 nm, which is considerably smaller compared to the lattice parameter and corresponds to an average of 2.5 stacked graphene sheets. A summary of the obtained and calculated values is given in Table 4.5.

Table 4.5: Lattice parameters obtained from the WAXS patterns presented in Fig. 4.6a and b.

Material	$Q_{(002)}$ (nm^{-1})	$d_{(002)}$ (nm)	$Q_{(10)}$ (nm^{-1})	$d_{(10)}$ (nm)	a (nm)	c (nm)	L_a (nm)	L_c (nm)
AC-Fs	15.88	0.396	30.39	0.207	0.239	0.791	3.20	1.16
AC-CSS	-	-	30.56	0.206	0.238		2.90	-
AC-SCG	15.63	0.402	30.33	0.207	0.239	0.804	2.82	0.63

4.3.2 Small-angle X-ray scattering

The analysis of the SAXS patterns relies on the equations and methods derived in section 2.3.1. Applying those models to the measured patterns is not straightforward due to a plethora of reasons, yet a modified DAB-model (equation (4.4)) is useful to extract a characteristic parameter. This model is based on three different contributions to the SAXS intensity: (a) the DAB-model contribution (first term in the square bracket), (b) the simplified Ruland fluctuation term for high Q-vectors and (c) a power-law term in the low Q-regime to account for scattering by large particles also taking into account their rough surface [77–79].

$$I(Q) = V \cdot \left[\frac{G}{\left(\frac{1}{a^2} + Q^2\right)^2} + \frac{B}{Q^2} + \frac{P}{Q^\alpha} \right] + C \quad (4.4)$$

The parameter V accounts for the unknown sample volume and C measures a constant background contribution. The exponent α was evaluated beforehand by a power-law fit to minimize the fitting variables. The background contribution was constrained to be greater or equal to zero. The obtained Debye correlation length a can serve as a qualitative measure for characteristic lengths within the material. The SAXS pattern and the model fit of the AC-Fs is shown in Fig. 4.7. For values of the scatter vector greater than 3 nm^{-1} , the curve deviates from the power-law with an exponent of -2.7 and begins to converge to a constant value. A crude estimation of this inflection point at 3.5 nm^{-1} leads to the assumption that the pore scattering is only due to pores above 1.8 nm, which is reflected in the pore size distribution in Fig. 4.3 and Fig. 4.4. Pore sizes below this value are in principle found at higher scattering vectors, but those are masked by the constant background, which also evolves into the onset of the strong (002)-peak seen in this material. The Debye-length for the AC-Fs was found to be 0.91 nm.

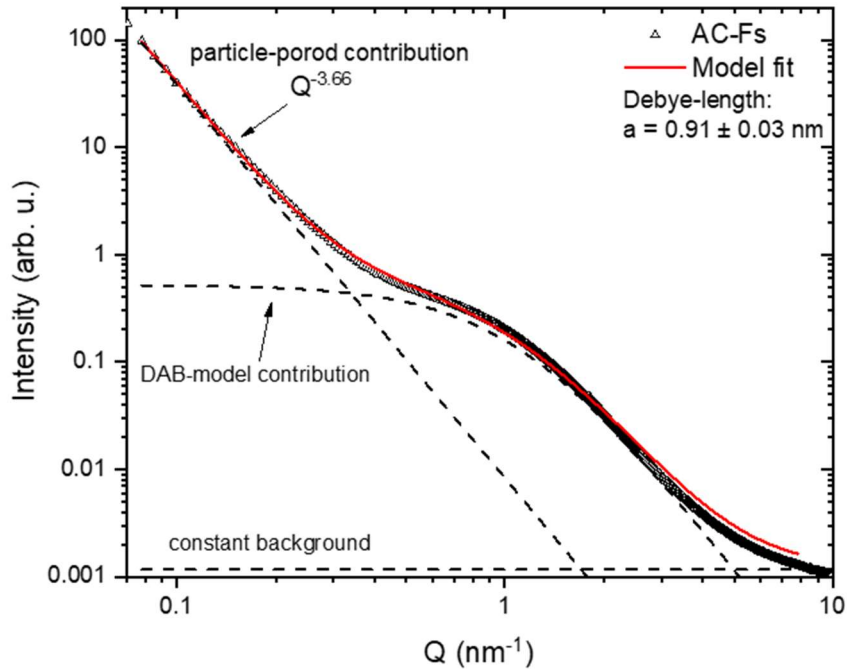


Fig. 4.7: SAXS pattern of the AC-Fs material and fitting with the model equation (4.4). The dashed lines show the different contributions to the fitted curve in red.

The measured intensity of the AC-CSS sample decays at high Q (4 to 9 nm^{-1}) with a power-law behavior of exponent 2.11, which is a little bit higher than the exponent of the density fluctuation term. The intensity is not converging towards a constant value up to 11 nm^{-1} , where at slightly higher Q the onset of the stacking peak would lead to a flattening of the curve. In the mid Q -regime the plateau is clearly developed, which correlates to a decrease in the Debye-correlation length ($a = 0.30$ nm). As seen at high scattering vectors (Fig. 4.8) the model fit deviates from the measured intensity. This is due to the overestimation of the constant background.

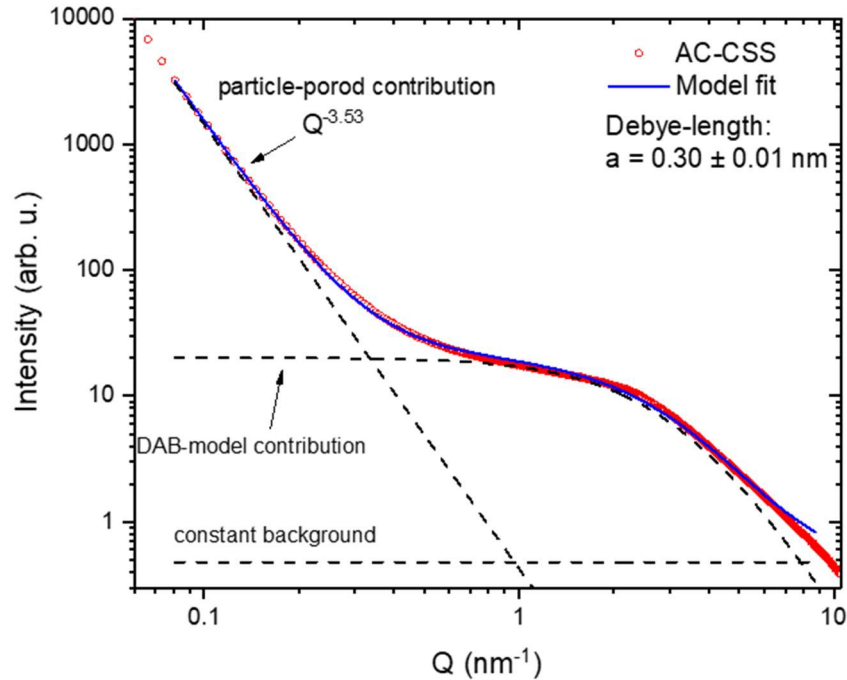


Fig. 4.8: SAXS pattern of the AC-CSS material and fitting with the model equation (4.4). The dashed lines show the different contributions to the fitted curve in blue.

The measured intensity of the AC-SCG material (Fig. 4.9) decays at high Q -values with a power-law exponent of exactly -2. This means that no sharp interfaces are present in this carbon structure and the scattering intensity is dominated by the fluctuations in interlayer spacing of the graphene sheets. The intensity does also not converge at high Q -vectors, but the fit is better in this range. This also reflects that the slope of the model fit at high Q is strongly influenced by the magnitude of the background, as it was zero in the case of AC-SCG.

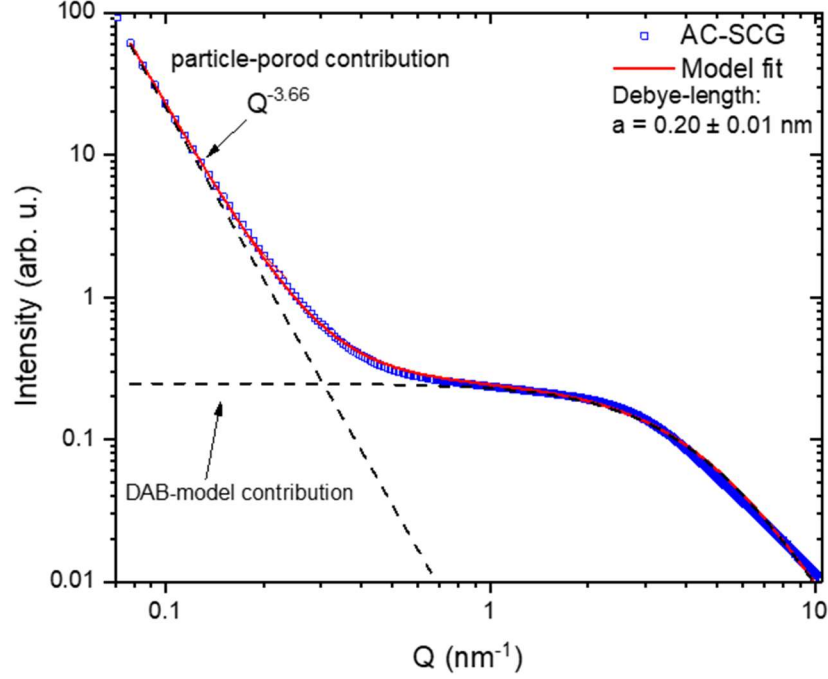


Fig. 4.9: SAXS pattern of the AC-SCG material and fitting with the model equation (4.4). The dashed lines show the different contributions to the fitted curve in red.

The parameter a (see equation (2.17)) was found to be 0.2 nm and could be linked to the porosity data as it theoretically equals the t -parameter from equation (2.26). Thus the average chord length of the pores $\langle l_{pore} \rangle$ and the carbon matrix $\langle l_{carbon} \rangle$ can be estimated under the assumption of a certain porosity φ . In fact, only the skeleton density ρ_{skel} has to be assumed, as it was not obtained experimentally. The porosity is then calculated by:

$$\varphi = \frac{\rho_{skel} \cdot V_{pore}}{(1 + \rho_{skel} \cdot V_{pore})}, \quad (4.5)$$

where V_{pore} is the obtained pore volume from N_2 or Ar gas sorption measurements. The skeleton density can be obtained from He-pycnometry or calculated from the lattice constant measured by XRD [53,55]. Prehal et al. have used the value of 1.9 g/cm³ (2.2

g/cm³ for graphite) for the skeleton density when constructing real space models of the porous carbon structure using SAXS data, which were in good agreement with the PSD obtained from gas sorption [56,57,78]. The pore volume might be chosen either as the total pore volume obtained by QSDFT or as a volume which accounts for pores below a certain size. The results for the total pore volume and for pore sizes below 2 nm are summarized in Table 4.6 and Table 4.7 for values obtained by N₂ and Ar gas sorption, respectively.

Table 4.6: Average chord lengths of carbon matrix and pores, calculated with the pore volume obtained by N₂ gas sorption.

Material	a (nm)	ρ_{skel} (g/cm ³)	$V_{pore,tot}$ (cm ³ /g)	φ (-)	$\langle l_{carbon} \rangle$ (nm)	$\langle l_{pore} \rangle$ (nm)	$V_{pore<2nm}$ (g/cm ³)	φ (-)	$\langle l_{carbon} \rangle_{<2nm}$ (nm)	$\langle l_{pore} \rangle_{<2nm}$ (nm)
AC-Fs	0.91	1.90	0.97	0.65	1.40	2.59	0.62	0.54	1.68	1.99
AC-CSS	0.30	1.90	1.57	0.75	0.40	1.19	1.27	0.71	0.42	1.02
AC-SCG	0.20	1.90	1.24	0.70	0.28	0.67	1.20	0.69	0.29	0.65

The average chord length values from the AC-Fs sample may be (over-)underestimated in case of the total pore volume, since the isotherms show external surface adsorption, which influences the pore volume. For pore sizes below 2 nm the average chord length of the pores is 1.99 nm, which is also reflected in the PSD and lies within the d_{25} and d_{50} values. The same accounts for the AC-CSS sample, where the average pore width is quite well met in the case of the total pore volume. In the case of the AC-SCG sample, $\langle l_{pore} \rangle$ is lower than the average pore width but is somewhere in between the pore sizes obtained by CO₂ gas sorption.

Table 4.7: Average chord lengths of carbon matrix and pores, calculated with the pore volume obtained by Ar gas sorption.

Material	a (nm)	ρ_{skel} (g/cm ³)	$V_{pore,tot}$ (cm ³ /g)	φ (-)	$\langle l_{carbon} \rangle$ (nm)	$\langle l_{pore} \rangle$ (nm)	$V_{pore < 2nm}$ (g/cm ³)	φ (-)	$\langle l_{carbon} \rangle$ (nm)	$\langle l_{pore} \rangle$ (nm)
AC-Fs	0.91	1.90	0.82	0.61	1.49	2.33	0.55	0.51	1.78	1.87
AC-CSS	0.30	1.90	1.57	0.75	0.40	1.19	1.31	0.71	0.42	1.05
AC-SCG	0.20	1.90	1.31	0.71	0.28	0.70	1.28	0.71	0.28	0.69

However, to compress the complexity of such pore structure into one parameter is not the best way to better understand it. For instance, stochastic models obtained by the Gaussian Random Field (GRF) model approach lead to a real space model of the pore structure and are therefore better suited to investigate carbon materials [57,77,78].

4.4 Hydrogen storage in biomass-derived activated carbon materials

In the following sections, the hydrogen uptake performance at different temperatures and the calculation of the enthalpy of adsorption is shown. Usually, the hydrogen uptake is presented with the gravimetric uptake calculated from the uptake in cm^3/g by:

$$\text{gravimetric uptake (wt\%)} = \frac{\text{uptake} \cdot M_{\text{H}_2} \left(\frac{\text{cm}^3}{\text{g}}\right)}{V_m \left(\frac{\text{cm}^3}{\text{mol}}\right) + M_{\text{H}_2} \cdot \text{uptake} \left(\frac{\text{cm}^3}{\text{g}}\right)} \cdot 100\% \quad (4.6)$$

Here, M_{H_2} is the molar mass of molecular hydrogen and V_m is the molar volume at STP conditions ($22.4 \text{ dm}^3/\text{mol}$). Towards the end of this section some correlation of structural parameters and the hydrogen uptake are shown.

4.4.1 Hydrogen uptake performance at different temperatures

The achievable hydrogen uptake strongly depends on the temperature and the applied pressure. For technical storage applications, temperatures between 77 K (liquid nitrogen temperature) and 112 K (liquified natural gas temperature), as well as pressures up to 100 bar are aimed to reach the DOE target. However, studying the uptake performance up to 1 bar can also help to correlate the structural characteristics to the uptake. Fig. 4.10a shows the hydrogen isotherms of the different samples at 77 K. The uptake performance for the AC-CSS and AC-SCG is very similar and was found to be 2.77 and 2.81 wt%, respectively. The AC-Fs sample exhibits a lower uptake of 1.47 wt%, but if normalized to the SSA (given in mmol/m^2) obtained by the QSDF method the difference in performance gets smaller. Yet, the other two samples exhibit nearly the same uptake, due to very similar SSAs and pore sizes. The H_2 uptake of AC-SCG is around 40 % higher compared to a similarly synthesized AC from spent coffee grounds (BET area of $1040 \text{ m}^2/\text{g}$, H_2 uptake of 1.75 wt% at 77 K and 1000 mbar), reported in the literature [80]. It can be further observed that the isotherms are far from reaching a

plateau and therefore measurements at higher pressures could reveal even greater storage capacities.

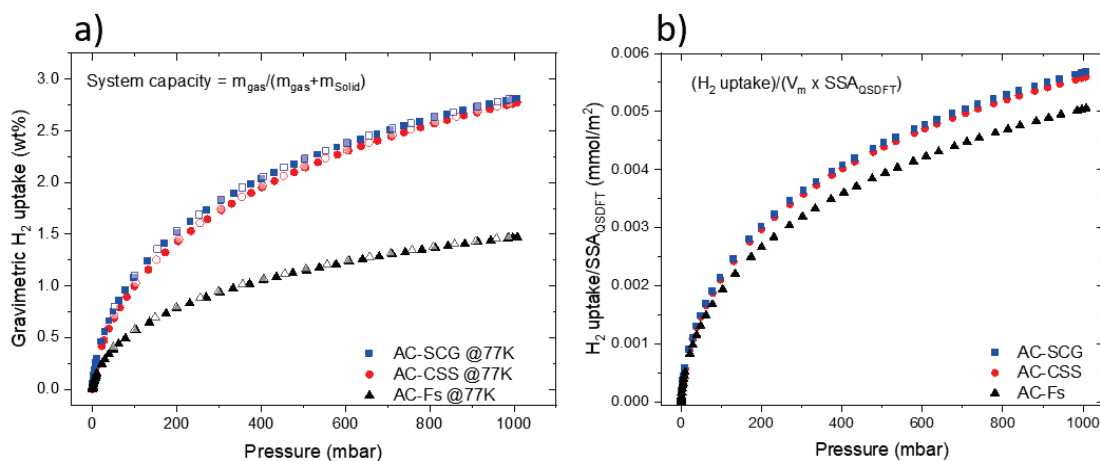


Fig. 4.10: a) Gravimetric hydrogen uptake of the different carbon materials at 77 K and b) hydrogen uptake in mmol per m² of surface area, calculated with the SSA obtained by the QSDFT method from the N₂ gas sorption data (Table 4.2).

The temperature dependency of the hydrogen uptake can be seen in Fig. 4.11d and is decreasing with increasing temperature. For a temperature increase from 77 to 87 K, the storage capacity drops by ~29 % for the AC-Fs and 27 % for AC-CSS and AC-SCG. By increasing the temperature up to 97 K, the hydrogen uptake is lowered by 50 % compared to the respective value at 77 K. This tremendous loss of capacity is one of the major hurdles for the application of such materials in cryo-compression systems, which may operate also at liquefied natural gas temperatures (~110 K). However, to improve the hydrogen uptake, a close look on the structural properties of the adsorbents and their connection to the uptake behavior is crucial. As discussed in section 2.2.3, the interaction strength between the hydrogen molecules and the carbon structure play an important role. At this point it is not possible to state a relation of the interaction strength as a function of the pore width, yet the average value as a function of the hydrogen uptake can be calculated.

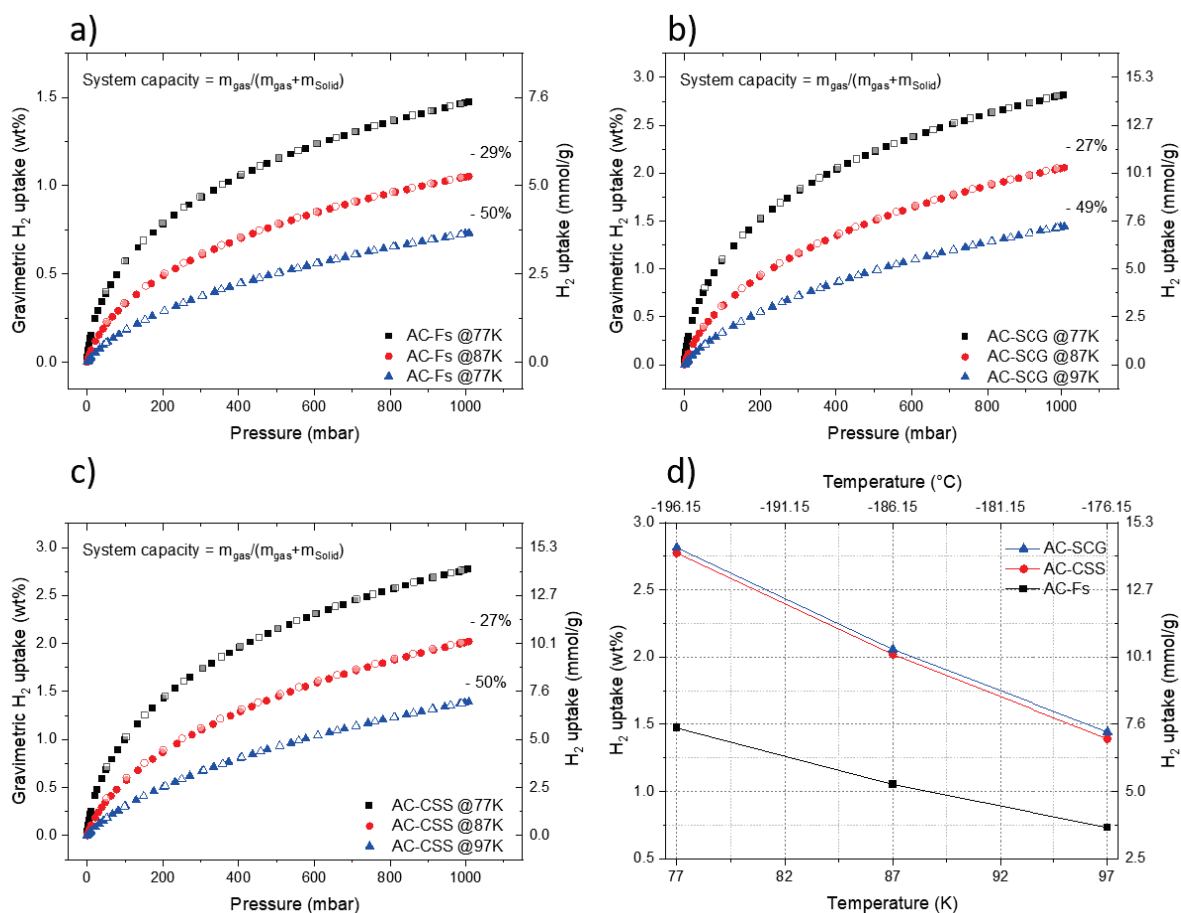


Fig. 4.11: Gravimetric hydrogen uptake for the biomass-derived carbons at a) 77 K, b) 87K and c) 97 K; percentages given in the plots show the decrease in maximum uptake at higher temperatures with respect to the uptake at 77 K and d) plot of the maximum uptake versus the operating temperature. The connection lines are intended for a better representation of the trend.

4.4.2 Isostatic enthalpy of adsorption

In order to calculate the interaction strength or the average value of the enthalpy of adsorption ΔH_{ads} as a function of the uptake, two different approaches were used, following the procedure presented in Ref. [40].

The first approach is based on the Clausius-Clapeyron equation (2.14) and fitting of the isotherm, displayed as uptake in mmol/g versus the pressure in kPa, with the Freundlich-Langmuir (FL) equation (2.13). After fitting the isotherms, the FL equation is rearranged (see equation (4.7)) and used to calculate the pressures at T_1 , T_2 and T_3 using the obtained values a , b and c for each temperature, respectively, at the same loading n .

$$p(n) = \sqrt{\frac{c \cdot n}{a \cdot b - n \cdot b}} \quad (4.7)$$

With this it is possible to compare the pressures at the same adsorbate uptakes, which is called the isosteric condition. Directly taking the uptake and pressure data pairs would certainly not lead to the isosteric conditions, since it is rather random whether the same uptakes are present at different temperatures. However, the enthalpy of adsorption is then evaluated from the slopes (m) of linear fits of pressure and temperature data pairs, displayed in a plot of $\ln(p)$ vs. $1/T$, and calculated by $\Delta H_{ads} = R \cdot m$, where R is the universal gas constant. Additionally to the assumptions of the FL equation, also the Clausius-Clapeyron equation has two prerequisites as it assumes a negligible volume of the adsorbed phase and an ideal behavior of the gas phase [40].

The second approach makes use of the virial equation (2.11) and requires less workarounds as the first approach. Here, the isotherms measured at different temperatures are fitted with a global fitting procedure, while using as few fitting parameters as possible. In the present case, five a_i and three b_i terms were used. The former one directly correlates to the isosteric enthalpy of adsorption by:

$$\Delta H_{ads}(n) = R \cdot \sum_{i=0}^m a_i \cdot n^i \quad (4.8)$$

The results obtained by the two methods are shown in Fig. 4.12a and b, respectively. On the first sight it becomes clear that there are huge differences in the calculated values at low uptakes. The high values around zero uptake followed by the step decrease of ΔH_{ads} can be explained by the fitting procedure, since the FL equation cannot satisfactorily fit the first few points of the isotherm. At higher uptakes, the results of both methods are in a similar range, due to equally good fits in this area.

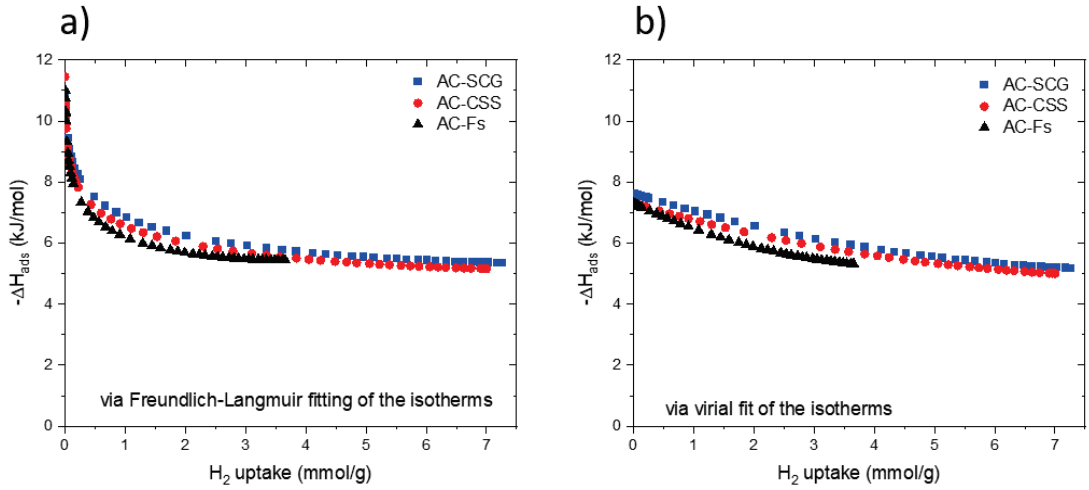


Fig. 4.12: Isosteric enthalpy of adsorption versus the hydrogen uptake for the different ACs; a) ΔH_{ads} calculated by fitting the isotherms with the Freundlich-Langmuir equation (right formula in equation (2.13)) and b) ΔH_{ads} calculated by global fitting of the isotherms with the virial equation (2.11).

The advantage of the virial analysis is the trustworthy value at almost zero hydrogen uptake (very low values of $\sim 10^{-5}$ mmol/g), which is referred to as the enthalpy of adsorption at zero coverage (ΔH_{ads}^0). The obtained average values (Table 4.8) for the virial analysis and also the zero coverage values are in good agreement with reported results obtained experimentally as well as from simulations [9,45,81]. However, the

measured hydrogen uptake is not correlated to the enthalpy of adsorption for these samples, but in general, the uptake increases with increasing interaction strength.

Table 4.8: Enthalpy and energy of adsorption values obtained from the two methods: (a) via the Freundlich-Langmuir equation and the Clausius-Clapeyron equation and (b) via the virial analysis.

Material	$-\overline{\Delta H}_{ads}^{(a)}$ (kJ/mol)	$-\overline{E}_{ads}^{(a)}$ (meV/molecule)	$-\overline{\Delta H}_{ads}^{(b)}$ (kJ/mol)	$-\overline{E}_{ads}^{(b)}$ (meV/molecule)	$-\Delta H_{ads}^0{}^{(b)}$ (kJ/mol)	$-E_{ads}^0{}^{(b)}$ (meV/molecule)
AC-Fs	8.23	85.3	6.31	65.4	7.30	75.7
AC-CSS	8.30	86.1	6.15	63.8	7.30	75.7
AC-SCG	8.05	83.5	6.40	66.3	7.63	79.1

$\overline{\Delta H}_{ads}$ denotes the isosteric enthalpy of adsorption and \overline{E}_{ads} the corresponding energy of adsorption of a single hydrogen molecule. ΔH_{ads}^0 and E_{ads}^0 denote the isosteric enthalpy and energy of adsorption at zero or very low surface coverage, respectively.

4.5 Hydrogen uptake and structural parameters

The H₂ uptake of porous materials cannot be linked to only one structural parameter and was found to depend on the surface area, the pore volume, the pore width and the distribution thereof. In the following pages, the measured H₂ uptakes at 77 K are presented together with those structural parameters.

4.5.1 Gas adsorption analysis and hydrogen uptake

Firstly, the values of the mean pore width d_{50} and the average pore width (APW, see equation (4.2), as derived by the QSDFT method, in respect to the hydrogen uptake normalized to the SSA of the samples are shown in Fig. 4.13. The hydrogen uptake per m² is increasing with decreasing mean (average) pore width. This reflects that narrow pores are the preferred adsorption sites for H₂ and a large pore volume with a narrow size distribution below < 1nm is beneficial to increase the storage capability of an AC as stated in section 4.5.1.

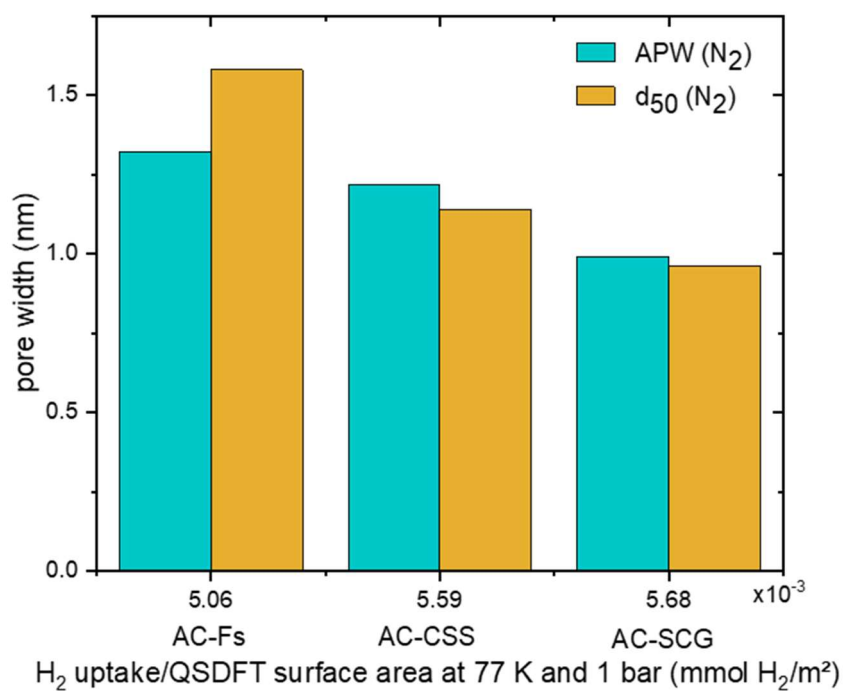


Fig. 4.13: Bar diagram presenting the mean pore width d_{50} and the average pore width (APW), as obtained by the QSDFT method using the N₂ gas sorption data, against the hydrogen uptake at 77 K and 1 bar normalized by the respective SSA obtained by QSDFT for the samples.

The combination of the PSDs (Fig. 4.14) obtained from Ar and CO₂ also reveals the lower mean pore width of the AC-SCG sample. This plot does not give a quantitative measure but provides a qualitative continuous PSD for pore sizes between 0.4 and 3 nm.

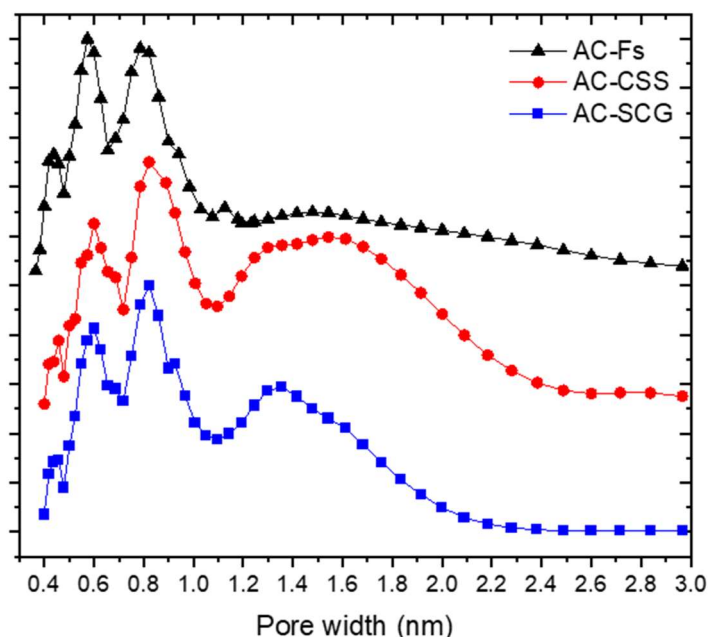


Fig. 4.14: Combined PSD obtained from merging the PSDs generated by QSDFT from the Ar and by GCMC from the CO₂ gas sorption data. The plot is presented in a qualitative manner and does not resemble a continuous PSD obtained by a single method and should therefore not be used to extract any quantitative relationships other than the position of the peaks. The merging was achieved by normalizing the individual PSDs to a common value of the cumulative pore volume at a certain pore width (0.57, 0.82 and 0.82 for the AC-Fs, AC-CSS and AC-SCG, respectively). The shown PSDs are shifted vertically for a better visualization.

The main difference between the PSDs can be seen in the range of 1-3 nm, as the AC-CSS exhibits also a notable amount of pores between 1 and 2.4 nm (broader distribution), whereas the AC-SCG sample shows only a narrower peak around 1.35 nm. This is also reflected by comparing the pore volume for pores < 2 nm and for those < 1 nm, which are 1.31 cm³/g and 0.46 cm³/g, respectively, for the AC-CSS and 1.28 cm³/g and 0.60 cm³/g, respectively, for the AC-SCG. The mean pore size of the AC-Fs sample is larger as the APW, which is related to the broad distribution of pore widths between 1 and 3.5 nm.

4.5.2 Characteristic lengths and hydrogen uptake

From the experimental methods used to characterize the samples, different structural lengths have been calculated, which basically condense the complexity of the pore system into a single parameter. From X-ray scattering in the wide-angle regime, as well as from Raman spectroscopy, the in-plane correlation length L_a and from the small-angle regime the average chord length of the pore $\langle l_{pore} \rangle$ were obtained. Those characteristic lengths are presented for each sample with respect to the hydrogen uptake at 77 K and 1 bar in Fig. 4.15.

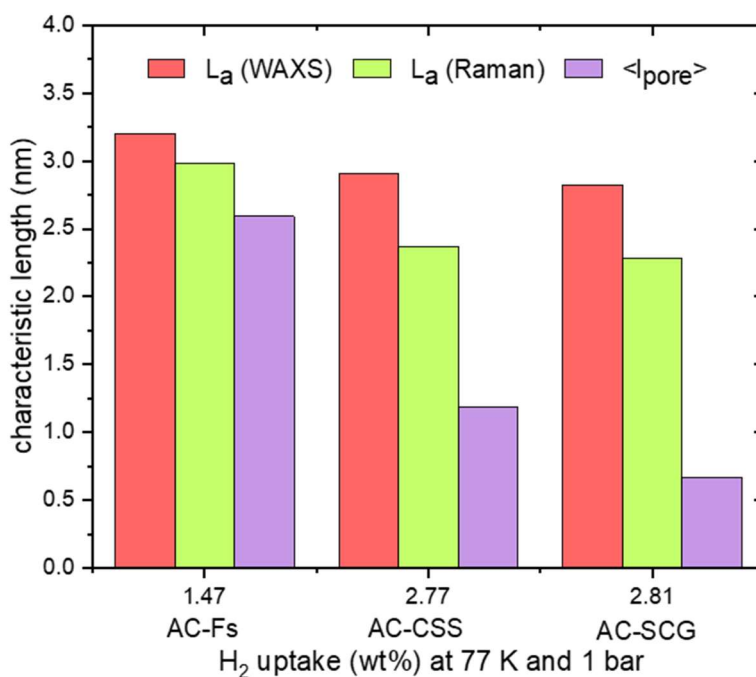


Fig. 4.15: Characteristic lengths of the samples obtained from WAXS, Raman spectroscopy and SAXS with respect to the hydrogen uptake.

With decreasing values of the characteristic lengths, the hydrogen uptake increases. The average chord length of the pores $\langle l_{pore} \rangle$ obtained from SAXS by assuming the skeleton density and using the pore volume obtained from N_2 gas adsorption also gives just a qualitative measure and cannot be directly related to the real pore structure. The used model to extract the Debye-length has not been tested up to this point and was also not

compared to similar parameters obtained by a different method. However, these values follow the common trend of increasing uptake with decreasing characteristic length.

The in-plane correlation length (or crystallite size) L_a also follows the same trend, as the hydrogen uptake increases with decreasing length. This value has a closer relation to the structural characteristic of the materials as it reflects the average length until which the periodicity of the 2D graphene lattice is preserved. In other words, it relates to the mean number of defects present in a certain area. From this point of view the introduction or presence of defects in the graphene lattice increases the interaction strength between the carbon matrix and the hydrogen molecules, which was in fact also found in simulations of graphene composed of penta- and octagons instead of hexagons (although the uptake was only moderately higher) [45,82]. From scattering alone, it is of course not possible to distinguish between the kinds of defects. Any further interpretations of the influence of the pore size, pore volume, surface area and role of defects in the structure on the hydrogen uptake may be subject to another thesis. Some methods on how to obtain a deeper insight into the hydrogen storage potential of activated nanoporous carbons is shortly covered in section 5.

4.6 Conclusions

The synthesis of nanoporous activated carbons from biological waste materials provides an outstanding opportunity to bring these materials back into commercial and sustainable use. The investigated activated carbons from spent coffee grounds, coffee silver skin and fines from paper production exhibit high surface areas and a high micropore volume, which makes them attractive to many different applications. The employed experimental methods have led to a better insight into the pore structure and the porosity properties, but further analysis in combination with simulations could lead to an even better understanding of the underlying structure and hydrogen uptake performance. The quite high hydrogen uptake at 77 K of the AC-SCG and the AC-CSS samples corresponding to 2.81 and 2.77 wt%, respectively, suggest a very good performance at elevated pressures, which has to be experimentally verified in the near future. The difference in uptake of the AC-Fs sample is explainable by the higher amount of pores with a width > 2 nm. However, the influence of the structural features of the precursor, as well as the influence of the conditions during the activation process, could also help to further improve the tailoring of the pore structure to enhance the hydrogen uptake.

Finally, the coffee derived carbons, due to their high hydrogen uptakes at ambient pressure together with the readily available amounts of waste material precursors make them promising potential candidates for potential use in cryo-compression hydrogen storage systems.

5 Summary and outlook

The ambitious goals of the Paris Agreement to keep the global average temperature increase below 2 °C requires a transition to renewable energy sources. This also means that the private transport needs to undergo a fundamental change, away from fossil fuel-driven vehicles to electrified cars. In the last couple of years many efforts have been made to prepare this transition and many big car manufacturers are battling to elevate the achievable range of electric cars using battery systems. An alternative is given by fuel cell powered cars, which use gaseous hydrogen as fuel, which upon development of a sophisticated storage system could outperform batteries. However, there is still a lot of work to be done, which is of technical and scientific nature. The underlying physics of the hydrogen adsorption in nanoporous materials, especially carbons, has been investigated experimentally and theoretically, yet there are some open questions to be answered in order to find the right structural parameters for a high storage capacity. From a scientific point of view the interaction of the two fundamental building blocks to all life on earth opens a plethora of different research activities.

The used experimental methods and the results obtained in the course of this thesis only represent a small snapshot of the greater picture. As stated in section 2.2.3, the use of neutrons to probe the interaction of hydrogen molecules and the carbon matrix allows to obtain a better insight into the density of the adsorbed molecules. The confinement of a species inside pores of a few Å in size changes the properties of the gas compared to the bulk state. Of which kind and magnitude these changes are could be explored by the combination of in-situ neutron scattering experiments and modeling of the carbon structure. With such in-situ SANS experiments it is possible to obtain the average density of the adsorbed phase as a function of external pressure and temperature [42]. Depending on the PSD of the investigated materials the density may be linked to a certain pore width, but this requires somehow a certain degree of uniformity thereof. The modelling of the carbon structure using the GRF approach can resemble the pore structure of nanoporous carbons quite well as shown by Prehal et. al. [56]. As neutrons are strongly scattered by hydrogen molecules the obtained in-situ SANS signal at different pressures

can be used to construct a real space model of the arrangement of the hydrogen molecules, which would resemble the pore structure. From these data not only the density of the adsorbed phase could be extracted but also the influence of the confinement. The use of deuterium gas (D_2) could reveal isotope effects, which may help to further improve theoretical models. Theoretically speaking a mixture of H_2 and D_2 in a certain ratio would result in a scattering length density (SLD) of almost zero, which opens the possibility to investigate the influence of the gas pressure on the carbon nanopore structure.

However, it would also be beneficial to know the density of the adsorbed phase only by means of gas adsorption isotherms collected at low pressures, which was somehow not considered in previous studies. One tool presented in the thesis, which is widely used, is to calculate the PSD from isotherms. The generalized adsorption isotherm (equation (2.7)) may be used to fit experimentally obtained H_2 isotherms while delivering pore size specific densities of the adsorbed phase. Please note that this is just a crude assumption and must be further developed and tested. Furthermore, inelastic neutron scattering (INS) could also add a great value to the knowledge of hydrogen behavior confined in nanopores. With this method it was found that the confined hydrogen can be densified up to the density of solid hydrogen under high applied pressures and confinement in narrow pores [46]. Additionally with quasi-elastic neutron scattering (QENS) it is possible to extract diffusion properties of the confined hydrogen molecules [13,23].

I now would like to close this thesis with a thought of mine constantly echoing in my head while writing these last few words:

“Ideas may arise along the way, but yet it is fortune who decides the time to shine”

6 Bibliography

- [1] United Nations, Paris Agreement.
ec.europa.eu/clima/policies/international/negotiations/paris_de#tab-0-1.
- [2] Y. Du Robiou Pont, M.L. Jeffery, J. Gütschow, J. Rogelj, P. Christoff, M. Meinshausen, *Nature Clim Change* 7 (2017) 38–43.
- [3] Christian Koczwara, Performance evaluation and in situ X-ray scattering of ordered mesoporous carbons for electrochemical energy storage applications, Leoben, 2019.
- [4] eurostat, Renewable energy statistics. ec.europa.eu/eurostat/statistics-explained/index.php?title=Renewable_energy_statistics.
- [5] statista.com, Pro-Kopf-Absatz von Kaffee in ausgewählten Ländern weltweit im Jahr 2019. de.statista.com/statistik/daten/studie/199898/umfrage/konsum-von-kaffee-in-europa/.
- [6] L.F. Ballesteros, J.A. Teixeira, S.I. Mussatto, *Food Bioprocess Technol* 7 (2014) 3493–3503.
- [7] Nikolaos Kostoglou, Carbon-based nanoporous materials for hydrogen storage, Leoben, 2017.
- [8] US Department of Energy, DOE Technical Targets for Onboard Hydrogen Storage for Light-Duty Vehicles. www.energy.gov/eere/fuelcells/doe-technical-targets-onboard-hydrogen-storage-light-duty-vehicles.
- [9] A. Züttel, *Die Naturwissenschaften* 91 (2004) 157–172.
- [10] J.F. Peters, M. Baumann, B. Zimmermann, J. Braun, M. Weil, *Renewable and Sustainable Energy Reviews* 67 (2017) 491–506.
- [11] M.C. McManus, *Applied Energy* 93 (2012) 288–295.
- [12] R. Moradi, K.M. Groth, *International Journal of Hydrogen Energy* 44 (2019) 12254–12269.

- [13] D.P. Broom, *Hydrogen Storage Materials: The characterisation of their storage properties*, Springer, London, 2011.
- [14] E. Boateng, A. Chen, *Materials Today Advances* 6 (2020) 100022.
- [15] J.O. Abe, A.P.I. Popoola, E. Ajenifuja, O.M. Popoola, *International Journal of Hydrogen Energy* 44 (2019) 15072–15086.
- [16] D.J. Durbin, C. Malardier-Jugroot, *International Journal of Hydrogen Energy* 38 (2013) 14595–14617.
- [17] R.K. Ahluwalia, J.K. Peng, *International Journal of Hydrogen Energy* 34 (2009) 5476–5487.
- [18] M. Hirscher (Ed.), *Handbook of hydrogen storage: New materials for future energy storage*, Wiley-VCH, Weinheim, 2010.
- [19] S. Niaz, T. Manzoor, A.H. Pandith, *Renewable and Sustainable Energy Reviews* 50 (2015) 457–469.
- [20] M. Sankir, N.D. Sankir, *Hydrogen Storage and Technologies*, John Wiley & Sons Incorporated, Newark, 2018.
- [21] US Department of Energy, *Materials-Based Hydrogen Storage*.
www.energy.gov/eere/fuelcells/materials-based-hydrogen-storage.
- [22] J. Ren, N.M. Musyoka, H.W. Langmi, M. Mathe, S. Liao, *International Journal of Hydrogen Energy* 42 (2017) 289–311.
- [23] K. Kaneko, F. Rodríguez-Reinoso, *Nanoporous Materials for Gas Storage*, 2019.
- [24] M. Thommes, K. Kaneko, A.V. Neimark, J.P. Olivier, F. Rodríguez-Reinoso, J. Rouquerol, K.S.W. Sing, *Pure and Applied Chemistry* 87 (2015) 1051–1069.
- [25] Gold APP Instruments.
gasadsorptiontech.wordpress.com/2016/01/08/nanomaterial-pore-types/.

- [26] S. Lowell, J.E. Shields, M.A. Thomas, M. Thommes, *Characterization of porous solids and powders: surface area, pore size and density*, Springer, Dordrecht, 2004.
- [27] G. Sdanghi, R.L.S. Canevesi, A. Celzard, M. Thommes, V. Fierro, *C 6* (2020) 46.
- [28] I. Cabria, *International Journal of Hydrogen Energy* 45 (2020) 5697–5709.
- [29] J.E. Lennard-Jones, *Physica* 4 (1937) 941–956.
- [30] Sebastian Stock, *About the crystalline structure and electronic properties of carbon*. Seminar paper, Lisbon, Portugal, 2020.
- [31] E. Malić, A. Knorr, S. Winnerl, *Graphene and carbon nanotubes: Ultrafast relaxation dynamics and optics*, Wiley-VCH, Weinheim, 2013.
- [32] K. Tanaka, S. Iijima (Eds.), *Carbon nanotubes and graphene*, 2nd ed., Elsevier, Amsterdam, Boston, Heidelberg, 2014.
- [33] M.A. Yahya, Z. Al-Qodah, C.Z. Ngah, *Renewable and Sustainable Energy Reviews* 46 (2015) 218–235.
- [34] S. Wang, D. Ábrahám, F. Vallejos-Burgos, K. László, E. Geissler, K. Takeuchi, M. Endo et al., *Langmuir the ACS journal of surfaces and colloids* 32 (2016) 5617–5622.
- [35] F. Banhart, J. Kotakoski, A.V. Krashennnikov, *ACS nano* 5 (2011) 26–41.
- [36] L.M. Malard, M.A. Pimenta, G. Dresselhaus, M.S. Dresselhaus, *Physics Reports* 473 (2009) 51–87.
- [37] G.A. Zickler, B. Smarsly, N. Gierlinger, H. Peterlik, O. Paris, *Carbon* 44 (2006) 3239–3246.
- [38] A.C. Ferrari, J.C. Meyer, V. Scardaci, C. Casiraghi, M. Lazzeri, F. Mauri, S. Piscanec et al., *Physical review letters* 97 (2006) 187401.

- [39] L. Peng, J.R. Morris, *J. Phys. Chem. C* 114 (2010) 15522–15529.
- [40] A. Nuhnen, C. Janiak, *Dalton transactions* (Cambridge, England 2003) 49 (2020) 10295–10307.
- [41] J.E. Sharpe, N. Bimbo, V.P. Ting, A.D. Burrows, D. Jiang, T.J. Mays, *Adsorption* 19 (2013) 643–652.
- [42] N.C. Gallego, L. He, D. Saha, C.I. Contescu, Y.B. Melnichenko, *Journal of the American Chemical Society* 133 (2011) 13794–13797.
- [43] L.J. Peng, J.R. Morris, *Carbon* 50 (2012) 1394–1406.
- [44] J.R. Morris, C.I. Contescu, M.F. Chisholm, V.R. Cooper, J. Guo, L. He, Y. Ihm et al., *J. Mater. Chem. A* 1 (2013) 9341.
- [45] M.N. Popov, T. Dengg, D. Gehringer, D. Holec, *C* 6 (2020) 20.
- [46] V.P. Ting, A.J. Ramirez-Cuesta, N. Bimbo, J.E. Sharpe, A. Noguera-Diaz, V. Presser, S. Rudic et al., *ACS nano* 9 (2015) 8249–8254.
- [47] Christian Prehal, *Ion electrosorption in nanoporous carbons*, Leoben, 2017.
- [48] J. Als-Nielsen, Des McMorrow, *Elements of modern X-ray physics*, 2nd ed., Wiley, Chichester, 2011.
- [49] O. Glatter, *Scattering Methods and their Application in Colloid and Interface Science*, Elsevier Science, San Diego, 2018.
- [50] P. Debye, H.R. Anderson, H. Brumberger, *Journal of Applied Physics* 28 (1957) 679–683.
- [51] Y.B. Melnichenko, *Small-angle scattering from confined and interfacial fluids: Applications to energy storage and environmental science*, Springer, Cham, 2016.
- [52] W. Ruland, *J Appl Crystallogr* 4 (1971) 70–73.

- [53] C.J. Jafta, A. Petzold, S. Risse, D. Clemens, D. Wallacher, G. Goerigk, M. Ballauff, *Carbon* 123 (2017) 440–447.
- [54] R. Perret, W. Ruland, *J Appl Crystallogr* 1 (1968) 308–313.
- [55] C. Koczwarra, S. Rumswinkel, L. Hammerschmidt, M. Salihovic, M.S. Elsaesser, H. Amenitsch, O. Paris et al., *ACS Appl. Energy Mater.* 2 (2019) 5279–5291.
- [56] C. Prehal, S. Grätz, B. Krüner, M. Thommes, L. Borchardt, V. Presser, O. Paris, *Carbon* 152 (2019) 416–423.
- [57] C. Prehal, C. Koczwarra, N. Jäckel, A. Schreiber, M. Burian, H. Amenitsch, M.A. Hartmann et al., *Nat Energy* 2 (2017).
- [58] C. Santos, E. Senokos, J.C. Fernández-Toribio, Á. Ridruejo, R. Marcilla, J.J. Vilatela, *J. Mater. Chem. A* 7 (2019) 5305–5314.
- [59] F. Atamny, O. Spillecke, R. Schlögl, *Physical chemistry chemical physics PCCP* 1 (1999) 4113–4118.
- [60] O. Paris, *Structure and Multiscale Mechanics of Carbon Nanomaterials*, Springer Vienna, Vienna, 2015.
- [61] M. Ruike, T. Kasu, N. Setoyama, T. Suzuki, K. Kaneko, *J. Phys. Chem.* 98 (1994) 9594–9600.
- [62] W. Ruland, *Acta Cryst* 22 (1967) 615–623.
- [63] W. Ruland, B. Smarsly, *J Appl Crystallogr* 35 (2002) 624–633.
- [64] M.A. Hobisch, J. Bossu, D. Mandlez, S.M. Bardet, S. Spirk, R. Eckhart, W. Bauer, *Cellulose* 26 (2019) 6933–6942.
- [65] G.Y. Gor, M. Thommes, K.A. Cychosz, A.V. Neimark, *Carbon* 50 (2012) 1583–1590.
- [66] J.S. Pedersen, *J Appl Crystallogr* 37 (2004) 369–380.

- [67] A. Eckmann, A. Felten, A. Mishchenko, L. Britnell, R. Krupke, K.S. Novoselov, C. Casiraghi, *Nano letters* 12 (2012) 3925–3930.
- [68] C. Casiraghi, F. Piazza, A.C. Ferrari, D. Grambole, J. Robertson, *Diamond and Related Materials* 14 (2005) 1098–1102.
- [69] M.J. Matthews, M.A. Pimenta, G. Dresselhaus, M.S. Dresselhaus, M. Endo, *Phys. Rev. B* 59 (1999) R6585-R6588.
- [70] M.A. Pimenta, G. Dresselhaus, M.S. Dresselhaus, L.G. Cançado, A. Jorio, R. Saito, *Physical chemistry chemical physics PCCP* 9 (2007) 1276–1291.
- [71] N. Kostoglou, I. Emre Gunduz, T. Isik, V. Ortalan, G. Constantinides, A.G. Kontos, T. Steriotis et al., *Materials & Design* 144 (2018) 222–228.
- [72] A. Habibi, S.M.M. Khoie, F. Mahboubi, M. Urgan, *Thin Solid Films* 621 (2017) 253–258.
- [73] C. Saringer, C. Oberroither, K. Zorn, R. Franz, C. Mitterer, *Journal of Vacuum Science & Technology A: Vacuum, Surfaces, and Films* 36 (2018) 21501.
- [74] A.C. Ferrari, J. Robertson, *Phys. Rev. B* 61 (2000) 14095–14107.
- [75] P. Ruz, S. Banerjee, M. Pandey, V. Sudarsan, P.U. Sastry, R.J. Kshirsagar, *Solid State Sciences* 62 (2016) 105–111.
- [76] S. Dantas, K.C. Struckhoff, M. Thommes, A.V. Neimark, *Carbon* 173 (2021) 842–848.
- [77] C.J. Gommers, T. Asset, J. Drnec, *J Appl Crystallogr* 52 (2019) 507–519.
- [78] C. Prehal, H. Fitzek, G. Kothleitner, V. Presser, B. Gollas, S.A. Freunberger, Q. Abbas, *Nature communications* 11 (2020) 4838.
- [79] L. He, Y.B. Melnichenko, N.C. Gallego, C.I. Contescu, J. Guo, J. Bahadur, *Carbon* 80 (2014) 82–90.

- [80] K.C. Kemp, S.B. Baek, W.-G. Lee, M. Meyyappan, K.S. Kim, *Nanotechnology* 26 (2015) 385602.
- [81] R. Roszak, L. Firlej, S. Roszak, P. Pfeifer, B. Kuchta, *Colloids and Surfaces A: Physicochemical and Engineering Aspects* 496 (2016) 69–76.
- [82] I.A. Baburin, A. Klechikov, G. Mercier, A. Talyzin, G. Seifert, *International Journal of Hydrogen Energy* 40 (2015) 6594–6599.